



# Linking Danube River activity to Alpine Ice-Sheet fluctuations during the last glacial (ca. 33–17 ka BP): Insights into the continental signature of Heinrich Stadials

Ruth Martinez-Lamas<sup>a, b, \*</sup>, Samuel Toucanne<sup>b, \*\*</sup>, Maxime Debret<sup>a</sup>, Vincent Riboulot<sup>b</sup>, Julien Deloffre<sup>a</sup>, Audrey Boissier<sup>b</sup>, Sandrine Cheron<sup>b</sup>, Mathilde Pitel<sup>b</sup>, Germain Bayon<sup>b</sup>, Liviu Giosan<sup>c</sup>, Guillaume Soulet<sup>b</sup>

<sup>a</sup> Normandie Univ., UNIROUEN, UNICAEN, CNRS, M2C, F-76000, Rouen, France

<sup>b</sup> IFREMER, Unité de Recherche Géosciences Marines, F-29280, Plouzané, France

<sup>c</sup> Department of Geology and Geophysics, Woods Hole Oceanographic Institution, 266 Woods Hole Road, Woods Hole, MA, 02543, USA

## ARTICLE INFO

### Article history:

Received 8 August 2019

Received in revised form

10 December 2019

Accepted 12 December 2019

Available online xxx

### Keywords:

Danube river

Floods

Hyperpycnites

Alpine ice sheet

Heinrich stadials

Seasonality

Black sea

## ABSTRACT

Offshore archives retrieved from marine/lacustrine environments receiving sediment from large river systems are valuable Quaternary continental records. In the present study, we reconstruct the Danube River activity at the end of the last glacial period based on sedimentological, mineralogical and geochemical analyses performed on long-piston cores from the north-west Black Sea margin. Our data suggest that the Danube River produced hyperpycnal floods throughout the ca. 33–17 ka period. Four main periods of enhanced Danube flood frequency, each of 1.5–3 kyr duration, are recorded at ca. 32.5–30.5 ka (equivalent to the first part of Heinrich Stadial –HS– 3), at ca. 29–27.5 ka (equivalent to Greenland Stadial 4), at ca. 25.3–23.8 ka (equivalent to HS 2) and at ca. 22.3–19 ka. Based on mineralogical and geochemical data, we relate these events to enhanced surface melting of the Alpine Ice Sheet (AIS) that covered ~50,000 km<sup>2</sup> of the Danube watershed at the Last Glacial Maximum (LGM). Our results suggest that (i) the AIS growth from the inner Alps to its LGM position in the northern Alpine foreland started from ca. 30.5 ka, ended no later than ca. 25.3 ka, and was interrupted by a melting episode ca. 29–27.5 ka; (ii) the AIS volume drastically decreased from ca. 22.3 to 19 ka, as soon as summer insolation energy at the AIS latitude increased; and (iii) HSs strongly impacted the AIS mass balance through enhanced summer surface melt. This, together with evidence of severely cool winters and the rapid expansion of sea ice in the North Atlantic, implies strong seasonality in continental Europe during stadials.

© 2019 Elsevier Ltd. All rights reserved.

## 1. Introduction

Fluvial landforms and sediments can be used to reconstruct past hydrological conditions since rivers are highly sensitive to environmental changes (Blum and Törnqvist, 2000; Macklin et al., 2012). Prominent examples from the British Isles (Macklin et al., 2005; Macklin and Lewin, 2003) and continental Europe

(Busschers et al., 2007; Gábris and Nádor, 2007; Gibbard, 1988; Kasse et al., 2010; Macklin et al., 2006; Mol et al., 2000; Pastre et al., 2003; Starkel et al., 2015; Vandenberghe, 2002) point to the impact of Quaternary climate change on river system dynamics. However, the riverine archives are highly complex (e.g. spatially-dependant types and rates of sedimentation, hiatus and erosion, difficulties in dating; Blum and Törnqvist, 2000; Coulthard et al., 2005; Macklin and Lewin, 2003; Vandenberghe, 2003). Hence the use of sediment archives retrieved offshore of large river systems can provide complementary high-frequency sediment flux records resulting from river discharge and climate variability (Simpson and Castelltort, 2012). This has been demonstrated in various geographic and climatic settings (e.g. Bonneau et al., 2014; Covault et al., 2011; Goodbred and Kuehl, 2000; Revel et al., 2010), including

\* Corresponding author. Normandie Univ., UNIROUEN, UNICAEN, CNRS, M2C, F-76000, Rouen, France.

\*\* Corresponding author.

E-mail addresses: [ruth.martinez-lamas1@univ-rouen.fr](mailto:ruth.martinez-lamas1@univ-rouen.fr) (R. Martinez-Lamas), [stoucann@ifremer.fr](mailto:stoucann@ifremer.fr) (S. Toucanne).

the giant glaciated catchments of European rivers, i.e. the Channel River (Ménot et al., 2006; Toucanne et al., 2009; Zaragosi et al., 2001) and the Dniepr River (Soulet et al., 2013). These studies provided remarkable new insights into the paleohydrology of Europe during past glacial intervals as well as into the impact of the Fennoscandian Ice Sheet (FIS) in amplifying, pacing and driving regional and global climate changes (e.g. Boswell et al., 2019; Soulet et al., 2013; Toucanne et al., 2015).

It is well-known that the Black Sea received vast amounts of sediment and meltwater from the Alpine Ice Sheet (AIS) and FIS during glacial periods (Bahr et al., 2006; Gorlach et al., 2017; Grosswald, 1980; Major et al., 2006; Mangerud et al., 2004; Soulet et al., 2013, 2011a; Tudryn et al., 2016). The Red Layers (e.g. Bahr et al., 2006), deposited in the north-west Black Sea by the Dniepr River and the retreating FIS between ca. 17.2 and  $15.7 \pm 0.3$  ka BP (Soulet et al., 2013), constitute a prominent example further highlighting the ability for ice-sheets to impact sediment routing systems down to the deep sea 'sink' (Jaeger and Koppes, 2016). By comparison, the impact of AIS fluctuation on the Danube River discharge and Black Sea sedimentary system has received much less attention. Yet, the entire north-east part of the AIS (~50,000 km<sup>2</sup>) drained into the Black Sea and sediment accumulated in the Danube delta (Giosan et al., 2006, 2005; Panin et al., 1983) and deep-sea fan (Constantinescu et al., 2015; Lericolais et al., 2013; Popescu et al., 2001; Wong et al., 1994) must have recorded Danube River activity and AIS fluctuations during the late Quaternary. Here, we provide a continuous, high-resolution record of the Danube River discharge into the Black Sea 'Lake' at the end of the last glacial period (from ca. 33 ka) through the study of two sediment cores retrieved midway between the Danube delta and the Danube deep-sea fan (Fig. 1). Millennial-scale variability in sediment input and source observed in our multi-proxy records suggests rapid regional-scale glacier fluctuations in the north-eastern Alps over the course of the AIS to its maximum extent and during the deglaciation.

## 2. Geological and environmental settings

### 2.1. The north-west Black Sea and the danube sediment routing system

Since its opening during the Upper Cretaceous, the Black Sea basin acts as a large sediment catchment area that accumulated a thick sedimentary cover of ~19 km in its western margin. Since the Pliocene, a 2.5 to 3 km-thick prograding depositional wedge has been formed by Danube and Dniepr sedimentary supplies (de Leeuw et al., 2018; Nikishin et al., 2003). This geological feature, forming the wide north-west Black Sea continental shelf (<140–170 m water depth) and margin, is incised by numerous erosive canyons (Riboulot et al., 2017) including the Danube Canyon which deeply incises the shelf over 26 km down to ~110 m water depth (Popescu et al., 2004) (Figs. 1 and 2). The Danube Canyon has fed an extensive, deep depositional (turbidite) system (i.e. Danube deep-sea fan) at water depths greater than 2000 m (Lericolais et al., 2013; Popescu et al., 2001; Wong et al., 1994). It has been active during the last glacial period and until ca. 11.7 ka (Constantinescu et al., 2015) when the Black Sea was a giant freshwater lake and lowstand conditions (~90–120 m below the present sea level) dominated (Deuser, 1972; Lericolais et al., 2011; Ross et al., 1970; Ryan et al., 1997; Yanchilina et al., 2017). The Danube deep-sea fan thus represents the final sink of the Danube sediment routing system (Matenco and Andriessen, 2013) (Fig. 1), i.e. the integrated dynamical system connecting erosion in mountain catchments of western Central Europe to downstream deposition in the Black Sea.

The Danube River is the second longest river in Eurasia, with a

length of 2900 km from the Black Forest (Germany) to its delta (Romania) (Fig. 1), a drainage area of 801,000 km<sup>2</sup> and a modern sediment load estimated at 42–67 Mt per year (sediment yield: ~80 t km<sup>2</sup>.yr<sup>-1</sup>). Today, it constitutes by far the main sediment source for the northern Black Sea considering the low sediment load, estimated to be less than 10 Mt per year in total, for the rivers Dniestr (sediment yield: ~30 t km<sup>2</sup>.yr<sup>-1</sup>), Dniepr and Don (sediment yield: ≤5 t km<sup>2</sup>.yr<sup>-1</sup>). This difference is due to the mountainous character of the Danube drainage area in comparison to the lowlands-dominated Dniestr, Dniepr and Don watersheds (Milliman and Farnsworth, 2013; Milliman and Syvitski, 1992; Panin and Jipa, 2002; Sommerwerk et al., 2009). Indeed, the Danube River collects water and sediment from the mountainous areas of the northern and eastern Alps (up to 4049 m high at Piz Bernina; Fig. 3), the Dinarides and the Carpathians (Fig. 1), mainly formed of Variscan metamorphic and magmatic basements and Mesozoic calcareous rocks (Asch et al., 2005). In detail, from its source to its mouth, the Danube River receives the following: on its right bank, the tributaries Iller, Inn, Enns, Drava and Sava, originating in the Alps and the Dinarides, as well as the Velika Morava flowing from the Balkans; and on its left bank, the major tributaries Morava, rising in the Bohemian Forest, and Tisza, originating in the Carpathians, and the Jiu, Olt, Siret and Prut rivers, with sources in the Carpathians (Garnier et al., 2002) (Fig. 1). In addition to the riverine material from the mountainous areas, the glacial loess deposits constitute a significant additional sediment supply to the Danube sediment load, especially in the Pannonian (Middle Danube) and Dacic (Lower Danube) basins (Marković et al., 2015).

### 2.2. Paleoenvironmental changes in the danube drainage area

The loess and glacial sequences preserved in the Danube catchment provide information on the intensity of Alpine glaciations (Marković et al., 2015), with the first major glaciation in the Alps dating from Marine Isotope Stage (MIS) 22 (Muttoni et al., 2003). The (local) Last Glacial Maximum (LGM) in the Alps (Upper Würmian, MIS 2; Chaline and Jerz, 1984, Figs. 1 and 3) lasted from not later than ca. 24 to 20–19 ka (e.g. Ivy-Ochs, 2015; Ivy-Ochs et al., 2008; Monegato et al., 2017), with glaciers extending tens of kilometers out onto forelands and coalescing into huge (Rhine, Isar/Loisach, Inn, Salzach and Traun, from west to east) piedmont lobes (up to 700 m in thickness) in the Molasse Basin, Upper Danube (Ivy-Ochs, 2015; van Husen, 2000) (Fig. 3). This time period is coeval with peak loess accumulation rates in the Pannonian Basin (Fitzsimmons et al., 2012) and the development of the Duttendorf loess sequence in the Salzach palaeoglacier area (Starnberger et al., 2011). Recent compilation of <sup>10</sup>Be surface exposure dating and radiocarbon ages demonstrate that if LGM glaciers vanished rapidly from the foreland at ca. 20–18 ka, the initiation of retreat from their maximum positions occurred as soon as ca. 24–22 ka (Ivy-Ochs, 2015; Ivy-Ochs et al., 2004; Reber et al., 2014). Note that the timing for the growth and demise of cirque and cirque-valley glaciers in the western and southern Carpathians mountains matches that recognized in the northern Alps (Makos et al., 2018, 2014; 2013; Reuther et al., 2007).

In contrast, little is known about pre-LGM ice fluctuations (Ivy-Ochs et al., 2008). The Middle Würmian (MIS 4 and 3; Chaline and Jerz, 1984) is poorly preserved in the Alps due to the excavation of valleys by the LGM ice advance soon after ca. 33–32 ka (i.e. onset of the Upper Würmian, as redefined by Spötl et al., 2013). However, recent <sup>10</sup>Be data from the western Alps and the Rivoli-Avigliana end-moraine system (northern Italy) yield a minimum age of  $41.2 \pm 1.9$  ka (MIS 3) for pre-LGM glacier advance(s) in the Pô Valley (Ivy-Ochs et al., 2018). This age fits well with the deterioration of climatic conditions over the Alps after ca. 45 ka (Heiri et al., 2014;



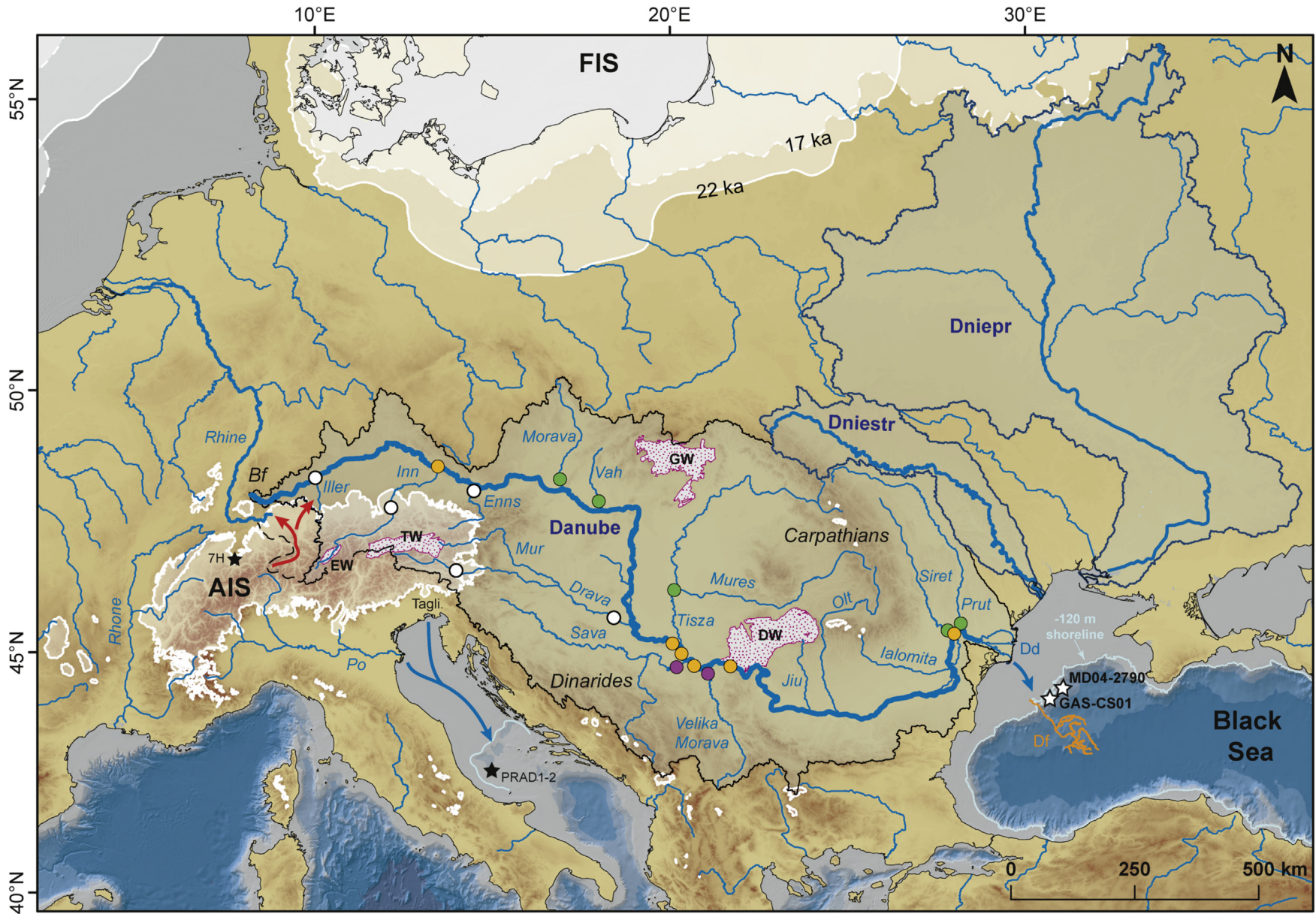


**Fig. 1.** Paleogeography of the Danube sediment routing system at the Last Glacial Maximum (LGM) including the Alpine Ice-Sheet (AIS, ~130,000 km<sup>2</sup>; Ehlers and Gibbard, 2004), the river course (~2900 km; ~801,000 km<sup>2</sup>) from the Black Forest (Bf) to the (modern) Danube delta (Dd), and the Danube deep-sea fan (Df; ~20,000 km<sup>2</sup>; Danube Canyon and channel-levees in orange) in the Black Sea 'Lake' (level ~90–120 m below the present sea level; paleoshoreline at ~120 m in the Black and Adriatic Seas in light blue). A significant part of the Rhine glacier (~14,000 km<sup>2</sup>; red arrows) drained into the Danube River at the LGM (Ellwanger et al., 2011), thus increasing the AIS surface in the Danube watershed to ~50,000 km<sup>2</sup>. Filled circles indicate the location of the modern river samples, with the colors referring to the Alpine (white), Dinaric (purple) and Carpathians (green) sources. Orange circles refer to the samples collected along the Danube mainstream (Table 3). Tagli.: Tagliamento glacier; EW: Engadine window; TW: Tauern window (Alps); GW: Gemer-Bürk window; DW: Danubian window (Carpathians). White stars in the Black Sea indicate the location of cores GAS-CS01 and MD04-2790. Black stars in the north-western Alps and the Adriatic Sea refer to the Sieben Hengste cave system (7H; Luetscher et al., 2015) and the PRAD1-2 borehole (Pellegriani et al., 2017, 2018) respectively. The limits of the Fennoscandian Ice Sheet (FIS) at 22 ka (continuous white line) and 17 ka (dashed white line) are also shown (Hughes et al., 2016). The retreat of the FIS in the upper Dniepr from ca. 17 ka caused the deposition of the Red Layers into the Black Sea (Soulet et al., 2013). Note the absence of an ice-sheet on the Carpathians at the LGM. (For interpretation of the references to color in this figure legend, the reader is referred to the Web version of this article.)



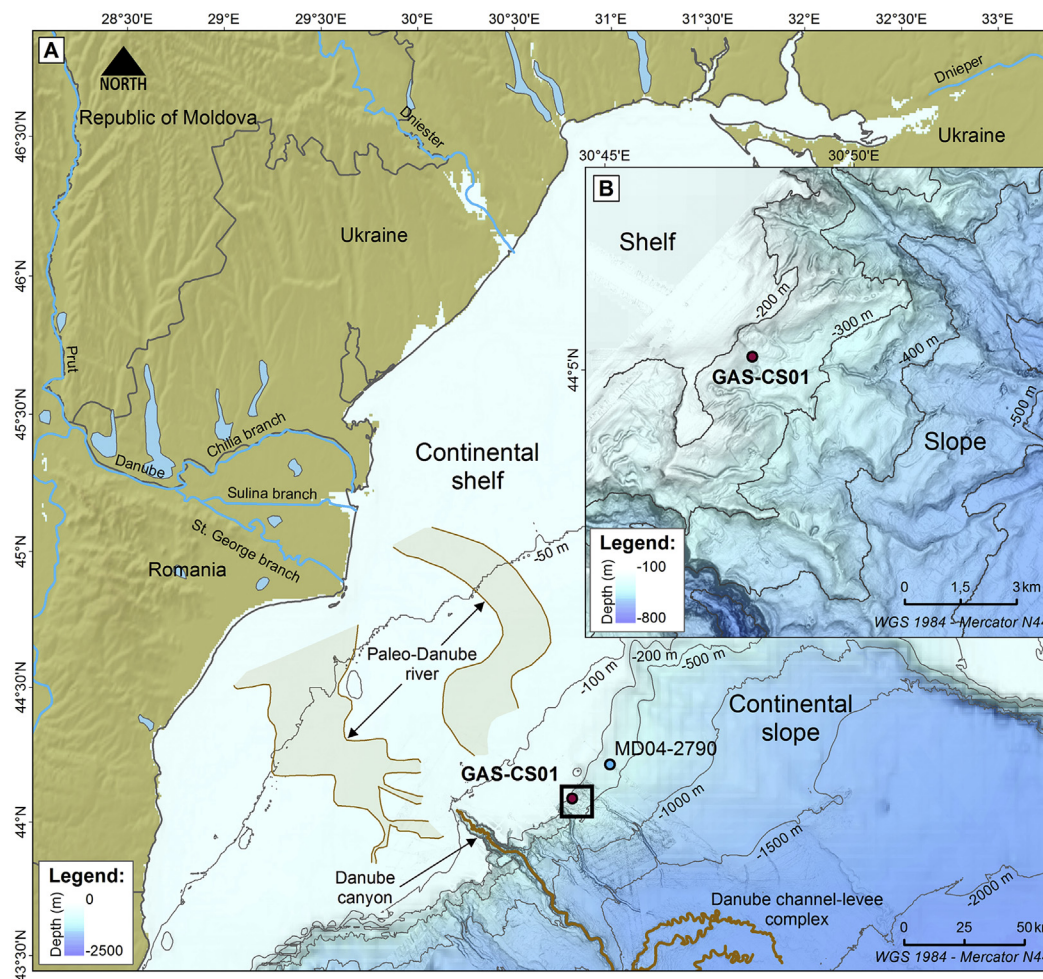


**Fig. 2.** Detailed map of the north-western Black Sea margin showing the location of the long-piston cores GAS-CS01 and MD04-2790 in front of the modern Danube delta. The numerous canyons (including the shelf-penetrating Danube Canyon; Popescu et al., 2004) visible on the continental slope are indicative of high Danube sediment discharge and of a good connectivity between the Danube delta and the shelf margin during the last glacial period, when the Black Sea was a giant freshwater lake and lowstand conditions dominated (see Part 2 for details). Danube paleovalleys from Popescu et al. (2004).

Starnberger et al., 2013). These results, including recent ones from the Berchtesgaden basin (Germany; Mayr et al., 2019), corroborate numerical simulations suggesting that a highly dynamic ice-sheet occupied the inner-Alpine regions throughout the last glacial period, with possible recurrent short-lived advances onto the forelands well before the LGM (Seguinot et al., 2018).

### 3. Materials

#### 3.1. Sediment cores

This study focuses on the Calypso long-piston cores GAS-CS01 (44°05.1'N, 30°47.5'E) and MD04-2790 (44°12.8'N, 30°59.6'E) retrieved from the north-west Black Sea margin (Figs. 1 and 2; Table 1). Core GAS-CS01 (33.4 m long) was collected at 240 m water depth from the shelf margin, ~40 km east of the Danube Canyon head, during the GHAAS oceanographic cruise (R/V Pourquoi Pas? Ker and Riboulot, 2015). Core MD04-2790 (30.3 m long) is located at 352 m water depth, ~19.6 km east of GAS-CS01. This core was collected during the ASSEMBLAGE-1 cruise (R/V Marion Dufresne; Lericolais, 2004) and has been extensively studied over the last few years for chronostratigraphical and paleoenvironmental studies (e.g. Soulet et al., 2011a, 2011b; Sanchi et al., 2014). Note that the length of cores GAS-CS01 (this study) and MD04-2790 (Soulet et al.,

2011a) has been corrected after removal of coring gaps (corrected length of 32.1 and 27.8 m, respectively). Core depths discussed in this study thus correspond to depth (cm, m) below sea floor (bsf), and corresponding depths (raw -cm- versus -cmbsf-) are presented in Tables 2 and 3.

#### 3.2. Danube River and tributary samples

In order to track paleoenvironmental changes in the Danube sediment routing system, eighteen riverine sediments have been recovered from the Danube River and its tributaries to compare their mineralogy with that of the GAS-CS01 core samples (Fig. 1; Table 3). Fine-grained river sediments constitute the mineralogical diversity of catchment areas. As such they can provide a reliable average mineralogical and geochemical composition of their corresponding drainage basin (Chamley, 1989; Sionneau et al., 2008). Considering the disproportionate role of mountains and glaciers in the erosion processes and the river sediment yields (Hallet et al., 1996; Milliman and Syvitski, 1992; Comiti et al., 2019), we mainly collected river sediments from tributaries draining the northern Alps (e.g. Iller, Inn;  $n = 5$ ), the western Carpathians (e.g. Tisza, Morava;  $n = 5$ ) and the Dinarides (Sava and Velika Morava rivers;  $n = 2$ ). Additional samples were collected along the Danube mainstream ( $n = 6$ ) from Passau (Germany) to the Black Sea, near



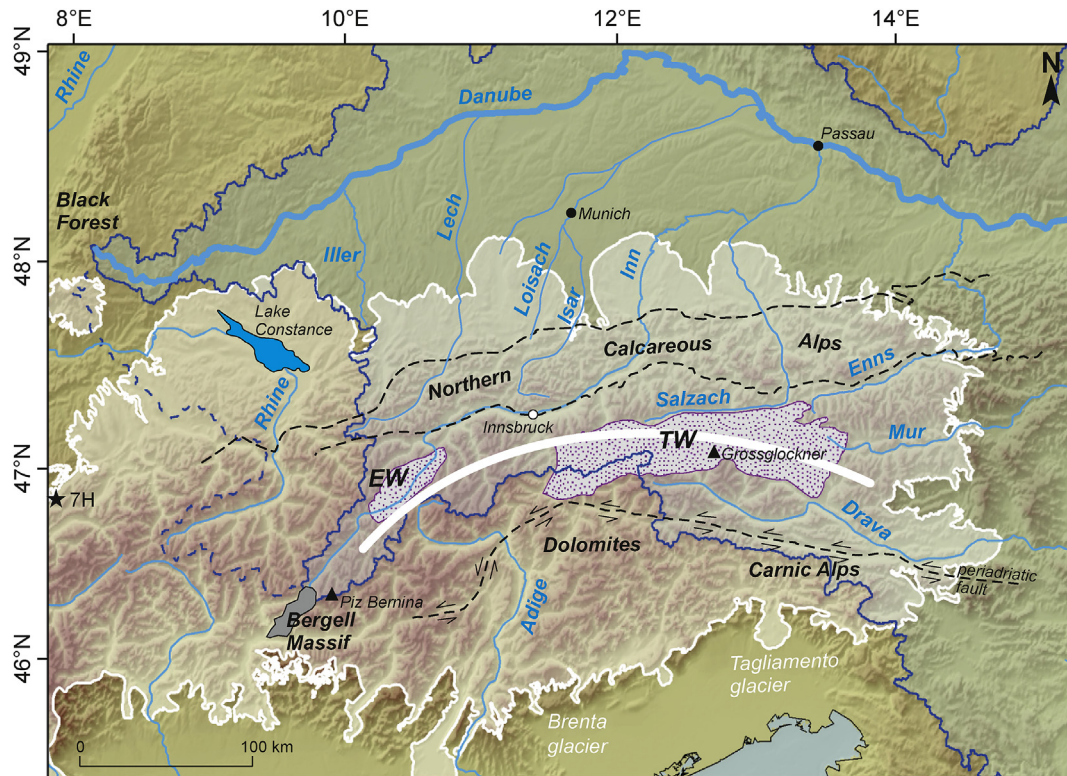


**Fig. 3.** Detailed map of the eastern Alps showing (i) the main geographical and geological features discussed in the main text, including the Tauern (TW) and Engadine (EW) windows (Bousquet et al., 2008); (ii) the main rivers (blue lines) draining into the Danube River (except the Rhine and Adige); (iii) the Alpine Ice-Sheet (AIS) at the LGM (Ehlers and Gibbard, 2004). The thick white line shows the AIS ice-divide at the LGM (based on Seguinot et al., 2018). Star labeled 7H: Sieben Hengste cave system (Luetscher et al., 2015). (For interpretation of the references to color in this figure legend, the reader is referred to the Web version of this article.)

**Table 1**  
Core locations.

Core Label	Lat. N	Long. E	Water depth (m)	Length (m)	Year	Cruise	IGSN
GAS-CS01	44,0865	30,7993	240	33,4	2015	GHASS	<a href="http://igsn.org/BFBGX-127384">http://igsn.org/BFBGX-127384</a>
MD04-2790	44,2219	30,9935	362	30,3	2004	ASSEMBLAGE-1	<a href="http://igsn.org/BFBGX-88381">http://igsn.org/BFBGX-88381</a>

**Table 2**  
New radiocarbon ( $^{14}\text{C}$ ) dates for cores GAS-CS01 and MD04-2790. Analyses were carried out at the Beta Analytic radiocarbon dating laboratory (USA).

Core ID	Depth (cm) <sup>a</sup>	Depth (cmbsf) <sup>b</sup>	Lab. Number	Sample type	$^{14}\text{C}$ age (yr BP)	error (1 $\sigma$ )
GAS-CS01						
GAS-CS01	1651	1614	Beta-440157	<i>Dreissena</i> sp.	24,920	120
GAS-CS01	1870	1831	Beta-440158	<i>Dreissena</i> sp.	25,070	120
GAS-CS01	2280	2238	Beta-463971	<i>Dreissena</i> sp.	25,710	110
GAS-CS01	2650	2604	Beta-463972	<i>Dreissena</i> sp.	26,220	110
GAS-CS01	2851	2796	Beta-479030	Organic matter	28,290	120
GAS-CS01	2853	2798	Beta-440160	<i>Dreissena</i> sp.	27,260	110
GAS-CS01	2955	2882	Beta-463973	Organic matter	28,700	140
GAS-CS01	3336	3214	Beta-479031	Organic matter	29,450	140
MD04-2790						
MD04-2790	2835	2600	Beta-477223	Organic matter	27,720	130
MD04-2790	3001	2765	Beta-463974	Organic matter	29,840	150

<sup>a</sup> Raw (i.e. uncorrected) depth in cores.

<sup>b</sup> Corrected depth in cores (i.e. after removal of gaps), in cm below sea floor (cmbsf).

the confluence with the Tisza and Velika Morava rivers. At every location where fine sediment was available, samples were collected from fresh bank deposit.

## 4. Methods

### 4.1. Core-scale analyses

The sedimentological analysis of GAS-CS01 is firstly based on

**Table 3**  
Clay mineralogy of the Danube River and its main tributaries. Geographic ‘mountainous’ clusters (raw - $\bar{x}$ - and weighted - $\bar{x}_w$ - mean values considering the river drainage surface, with the upper Drava excluded in the latter calculation) correspond to the main sediment sources of the Danube watershed. Note that the weighted mean clay mineralogy of these clusters (i.e. Alps + Dinarides + Carpathians) is close to that obtained for the Danube River mainstream.

River	Drainage area (km <sup>2</sup> )	Lat. N	Long. E	ICr (°Δ2θ)	Smectite (%)	Illite 2M1 (%)	Kaolinite (%)	Chlorite (%)	Dolomite (%)
<b>Danube Tributaries (n = 12)</b>									
<i>Alps (n = 5)</i>									
				$\bar{x}0.26 \pm 0.04$	$9.2 \pm 15.4$	$51.2 \pm 13.3$	$4.4 \pm 1.9$	$28.4 \pm 3.8$	$11.2 \pm 4.9$
				$\bar{x}_w0.28 \pm 0.04$	$12.2 \pm 16.2$	$44.7 \pm 12.6$	$5.6 \pm 2.2$	$27.8 \pm 3.9$	$9.6 \pm 5.8$
Iller	26,130	48,36232	10,00110	0,34	40	34	5	21	17
Inn	26,128	47,78181	12,12609	0,28	0	38	3	29	6
Enns	6185	48,21270	14,48660	0,23	3	65	3	30	17
Upper Drava	40,087	46,60046	13,89860	0,2	0	66	3	31	10
lower Drava	40,087	45,69050	18,41658	0,26	3	53	8	31	6
<i>Dinarides (n = 2)</i>									
				$\bar{x}0.3 \pm 0.04$	$25.5 \pm 14.5$	$44.5 \pm 9.5$	$17 \pm 0$	$14 \pm 5$	$1 \pm 1$
				$\bar{x}_w0.28 \pm 0.04$	$19.2 \pm 15.8$	$48.7 \pm 10.4$	$17 \pm 0$	$16.2 \pm 5.5$	$1.4 \pm 1.1$
Sava	95,793	44,72358	20,30960	0,26	11	54	17	19	2
Velika-Morava	37,571	44,60580	21,08620	0,34	40	35	17	9	0
				$\bar{x}0.3 \pm 0$	$44.2 \pm 25.5$	$34.4 \pm 15$	$11.8 \pm 7.2$	$9.4 \pm 4.5$	$0.8 \pm 0.8$
				$\bar{x}_w0.3 \pm 0$	$55.6 \pm 28$	$27.6 \pm 16.4$	$8.6 \pm 7.9$	$7.7 \pm 4.8$	$0.3 \pm 0.9$
<i>Carpathians (n = 5)</i>									
Morava	27,267	48,19118	16,97450	0,3	32	38	21	9	0
Tisza	15,609	46,14687	20,06457	0,3	55	28	8	8	0
Siret	46,289	45,39911	28,01163	0,3	66	22	5	7	1
Prut	28,568	45,47172	28,19500	0,3	68	22	5	5	1
Vah	1966	47,91403	18,01211	0,3	0	62	20	18	2
<i>Alps + Dinarides + Carpathians (351,593 km<sup>2</sup>)</i>									
				$\bar{x}0.28 \pm 0.01$	$29.6 \pm 19.1$	$40.4 \pm 9.2$	$10.9 \pm 4.9$	$16.6 \pm 8.3$	$3.3 \pm 4.2$
				$\bar{x}_w0.3 \pm 0.05$	$29.8 \pm 17.5$	$39.6 \pm 7.8$	$11 \pm 5.5$	$19.5 \pm 7.1$	$5.2 \pm 1$
<b>Danube River (n = 6)</b>									
Passau	801,093	48,59673	13,38283	0,39	3	41	23	33	0
Upstream Tisza	801,093	45,16503	20,10953	0,28	24	46	8	22	6
Upstream Sava	801,093	44,92347	20,32111	0,33	41	35	9	16	6
Downstream Sava	801,093	44,66575	20,78006	0,27	15	52	11	21	4
Moldava-Noua	801,093	44,69287	21,66701	0,29	42	37	7	14	4
Braila	801,093	45,32294	28,00246	0,25	54	27	8	11	6

visual description and X-ray images that allow the recognition of the main sedimentary facies and sequences, and the manual counting of laminae/beds (see Part 6.1; Fig. 4). 2D X-ray images were acquired with a Geotek XCT system (Ifremer, Brest) from split core sections. Detailed identification of the sedimentary facies was completed by hyperspectral reconstructed images. The hyperspectral spectroscopy technique consists of combining reflectance spectroscopy and digital imaging. A high-resolution digital image of a sediment core and a reflectance measurement for a specified wavelength range are collected in each pixel of the digital image. The wavelength intervals at which absorption features appear in their reflectance spectra are determined by the chemical compounds (e.g. organic matter) and physical properties (e.g. grain size) of the sediments (Debret et al., 2018; Jacq et al., 2019; Van Exem et al., 2019). In this study, we present high-resolution reconstructed images (spatial resolution of ~61 μm/pixel) in order to highlight the sedimentary features in GAS-CS01. Hyperspectral images were acquired at the University of Rouen (France) using a Specim (Spectral Imaging Ltd.) sediment-core-scanning system in combinations with a Specim PFD-xx-V10E camera (Specim Ltd., Finland) and OLES22.5 lens. These high-resolution images were acquired in the VNIR (Visible and Near InfraRed) spectral range between 400 and 1000 nm. The colour obtained with the VNIR is a false (highlighted) colour constructed after selecting three bands in the RGB system (697.94, 548.87 and 469.59 nm).

The bulk intensity of major elements for core GAS-CS01 was analysed using an Avaatech XRF core-scanner (Ifremer, Brest). XRF data were collected every 1 cm along the entire core, with a count time of 10 s, by setting the voltage to 10 kV (no filter) and 30 kV (Pd thick filter) and the intensity to 600 mA and 1000 mA, respectively. Millimetre-scale analyses were also conducted on some sections (30 s, 10–30 kV, 1000 mA) (Fig. 5).

The global mineralogy composition of GAS-CS01 sediments was determined by X-ray diffractometry (XRD), using a D8 Advance BRUKER model, a device type Bragg-Brentano equipped with a Cu

X-ray tube, a primary Soller slit of 0.6 mm, a nine-position sample holder and the VANTEC-1 Position Sensitive Detector with a nickel filter (Ni 0.5). Prior to analysis, dried sediment powders were inserted into the sample holder, and flattened. Measurements were made from 5 to 70° with a resolution of 0.01° lasting 1 s. The voltage and amperage were set up to 40 kV and 30 mA, respectively.

The clay mineralogy composition of GAS-CS01 sediments was determined by X-ray diffractometry (XRD), using a D2 PHASER BRUKER model, a Bragg-Brentano device type equipped with a Cu X-ray tube, a primary Soller slit of 0.6 mm and the LYNXEYE Detector with a nickel filter (Ni 0.5). In order to separate the clays from the rest of the matrix, the sample undergoes several stages of preparation: various chemical treatments to eliminate carbonates, iron oxides as well as the organic matter and a settling. Finally, these clays are plated on an oriented glass slide which is analysed in three different ways: without treatment, after saturation with ethylene glycol and after calcination at 490 °C. Measurements were made from 2 to 30° with a resolution of 0.02° lasting 1 s. The voltage and amperage were set to 30 kV and 10 mA, respectively. The illite crystallinity (ICr) index, or Kübler index (Kisch, 1991), was measured from XRD results. The illite crystallinity (°Δ2θ) is the full width at half maximum (FWHM) determined from the illite peak at 10 Å (Chamley, 1989). The clay mineralogy and the ICr of the riverine samples (n = 18) were also determined.

Finally, the geographical provenance of the GAS-CS01 sediments was determined measuring Nd isotopic ratios of fine-grained detrital fraction (n = 14). The neodymium isotopic composition (ε<sub>Nd</sub>) of terrigenous sediment is a powerful tracer for geographical provenance because the ε<sub>Nd</sub> signature of detrital sediment is retained during continental weathering and subsequent transport (Bayon et al., 2015; Goldstein and Jacobsen, 1988). We focus on the <63 μm fraction because the meltwaters of ice margins predominantly transport the clay and silt fractions of continental detritus (Boswell et al., 2018; Brown and Kennett, 1998). All bulk samples were first treated to quantitatively remove any biogenic, authigenic



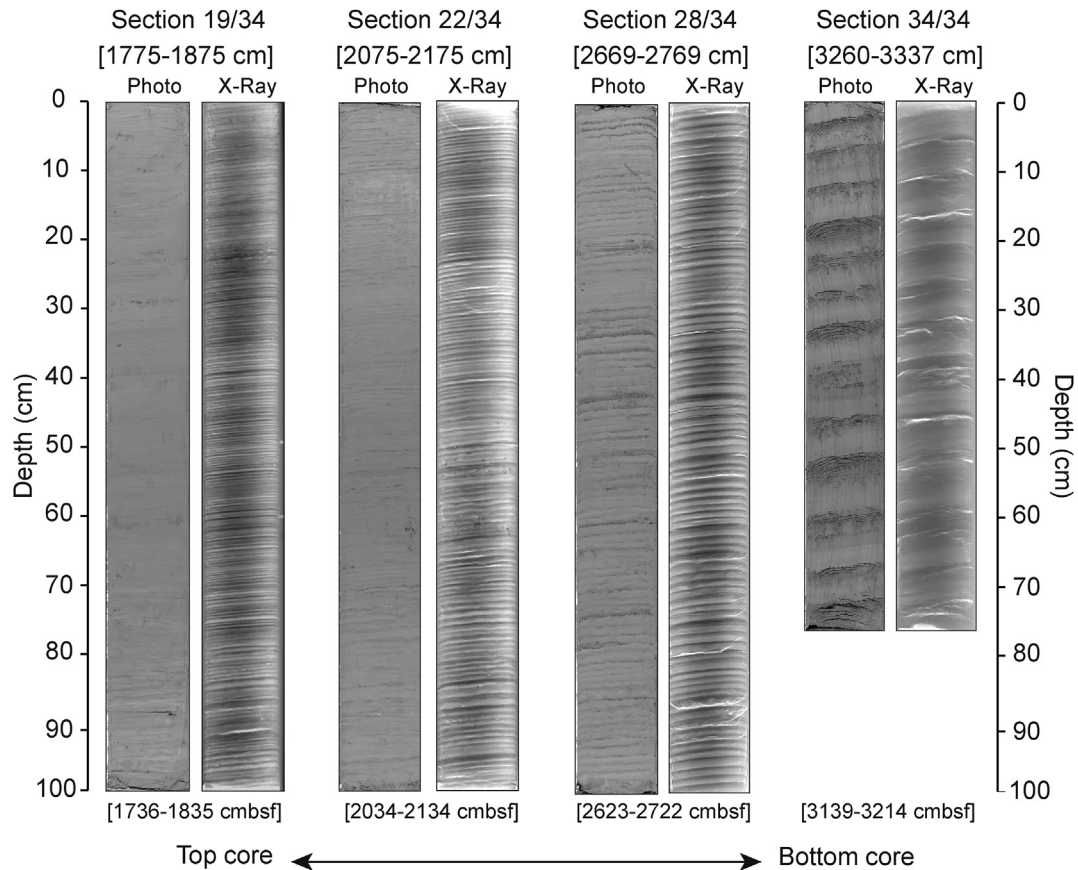


**Fig. 4.** Digital photographs and X-ray images of representative sections of the glacial sequence of core GAS-CS01 (i.e. 'banded lutites' -Unit III- of Ross and Degens, 1974). Note that the sequence is fully laminated, with clastic rhythmites evolving gradually downward from millimetre- (i.e. laminae; Scandinavian-type lacustrine varves of Degens et al., 1978) to decimetre-thick deposits (i.e. beds; megavarves of Degens et al., 1978). Clastic rhythmites in GAS-CS01 are interpreted as hyperpycnite sequences. See Figs. 7–9 for details.

and organic compounds (Bayon et al., 2002) and residual detrital fractions were digested by alkaline fusion prior to isolation of the Nd by ion-exchange chromatography (Bayon et al., 2009). Nd isotope measurements were performed on a Thermo Scientific Neptune MC-ICP-MS at the Pôle Spectrométrie Océan, Brest (France). Mass bias corrections on Nd were made with the exponential law, using  $^{146}\text{Nd}/^{144}\text{Nd} = 0.7219$ . Nd isotopic compositions were determined using sample-standard bracketing, by analysing an internal standard solution every two samples. Mass-bias corrected values for  $^{143}\text{Nd}/^{144}\text{Nd}$  were normalized to a JNdi-1 value. Replicate analyses of the JNdi-1 standard solution during the course of this study gave  $^{143}\text{Nd}/^{144}\text{Nd} = 0.512,113 \pm 0.000013$  (2SD,  $n = 28$ ), in full agreement with the reference value (0.512,115) of Tanaka et al. (2000), and corresponding to an external reproducibility of  $\sim \pm 0.25$   $\epsilon$ -units, taken as the estimated uncertainty on our measurements. In this study, both measured  $^{143}\text{Nd}/^{144}\text{Nd}$  ratios and literature data are reported in  $\epsilon_{\text{Nd}}$  notation  $[(^{143}\text{Nd}/^{144}\text{Nd})_{\text{sample}} / (^{143}\text{Nd}/^{144}\text{Nd})_{\text{CHUR}} - 1] \times 10^4$ , using  $(^{143}\text{Nd}/^{144}\text{Nd})_{\text{CHUR}} = 0.512,638$  (Jacobsen and Wasserburg, 1980). The  $\epsilon_{\text{Nd}}$  dataset available in core MD04-2790 for the ca. 28–10 ka period (Soulet et al., 2013) was produced using this procedure.

#### 4.2. Laminae-scale analyses

To characterize the sedimentary facies of core GAS-CS01, and the laminations in particular (see Part 6.1), we performed microscopic observations of 8 cm long thin-sections of impregnated sediments. The thin sections were prepared at the Université de Bordeaux

(UMR EPOC) according to the protocol described in Zaragosi et al. (2006). The studied intervals were selected from well-preserved and representative sedimentary facies (Fig. 4). The thin sections were then used for geochemical characterization of the sediments via scanning electron microscopy (SEM) at Ifremer, using a Thermo Scientific Quanta 200 equipped with an OXFORD Instrument X-MAXN silicon drift detector energy-dispersive X-Ray spectrometer (detector size: 80 mm<sup>2</sup>). The thin sections were coated with a thin layer of carbon and X-ray EDS maps acquired on an area of about 300 mm<sup>2</sup> to investigate the microscale geochemical distribution/composition of the sediments. Each area is composed of over 30 fields (3.47 × 3.04 mm each) scanned with a resolution of 1024 × 896 pixels (1 pixel = 3.4 μm). Additionally, morphological analyses of lithic grains were performed through SEM (Quanta 200). The grains were deposited onto SEM sample holders covered with a gold layer, and the SEM images were obtained with the secondary electron detector mode and an accelerating voltage of 5.0 kV.

Finally, we performed a total of 398 grain-size analyses using a Malvern Mastersizer 3000 laser diffraction particle size analyser (0.1–2000 μm) coupled with a Hydro LV wet dispersant unit. Ultrasonic dispersion (2 min) was conducted before analysis. The average resolution is 0.25 cm along the studied intervals.

#### 5. Age-depth model

Core chronologies based on radiocarbon dates are hampered in the Black Sea by unconstrained reservoir age (Guichard et al., 1993;

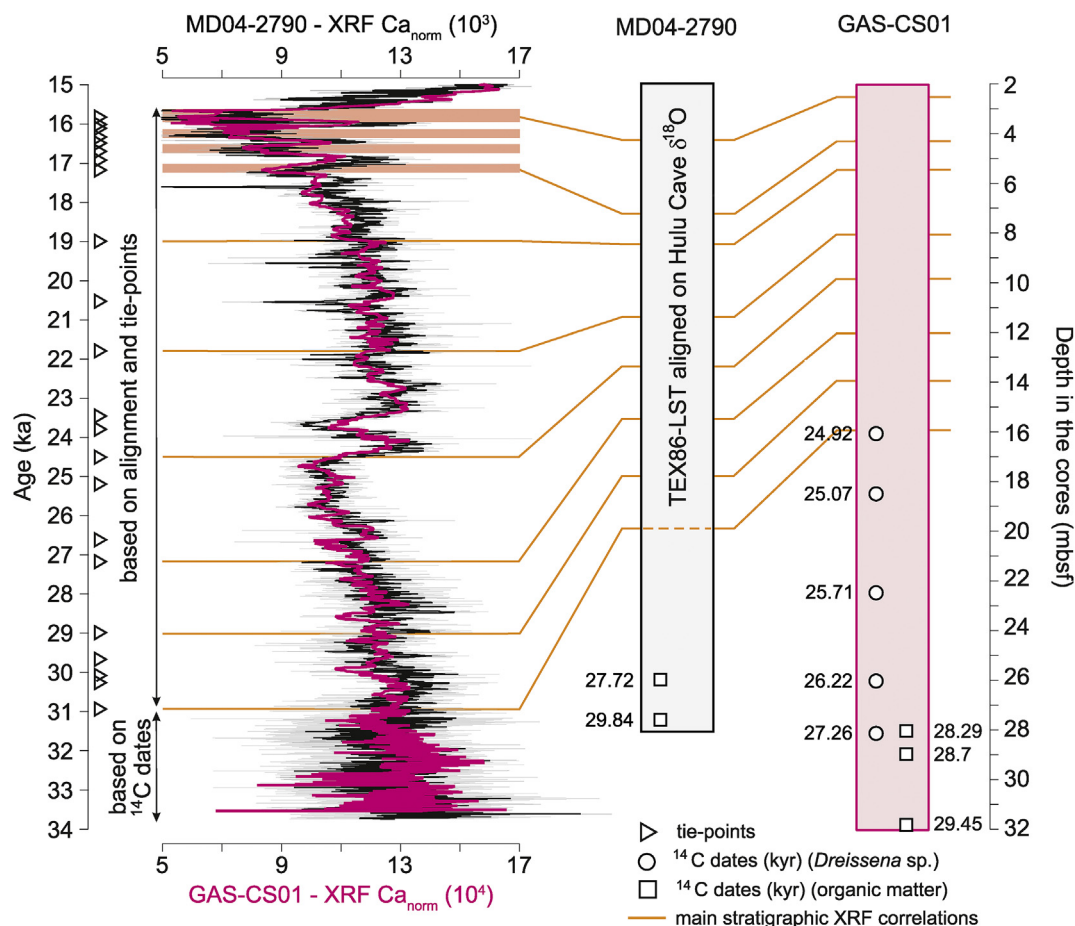


**Fig. 5.** Stratigraphic correlation between cores GAS-CS01 (magenta line) and MD04-2790 (black line; Soulet et al., 2011a) based on XRF- $\text{Ca}_{\text{norm}}$  profiles. See section 5 'Age-depth model' and Supplementary Online Material for details, and Table 2 for the radiocarbon dates.

Jones and Gagnon, 1994; Kwiecien et al., 2008; Soulet et al., 2011a, 2019). To circumvent the reservoir age issue, it is possible to reconstruct a meaningful environmental proxy from the core sediment and align it to a calendrically-dated reference record (e.g. Bard et al., 2004, 2013; Heaton et al., 2013; Skinner et al., 2010; Skinner et al., 2019; Soulet et al., 2011a) in order to obtain the calendar age-depth model without using radiocarbon dates. Original calendar age-depth model of core MD04-2790 is based on the alignment approach (Soulet et al., 2011a): TEX86-derived Lake Surface Temperature (LST) reconstructed from MD04-2790 sediments was aligned to Hulu Cave  $\delta^{18}\text{O}$  speleothem record (Wang et al., 2001). The GAS-CS01 calendar age-depth model is based on that of core MD04-2790, through the alignment of their respective XRF-Ca records (Fig. 5) which provided calendar ages at tie-points. The striking resemblance of XRF-Ca records confirms that the XRF  $\text{Ca}_{\text{norm}}$  is a basin-wide stratigraphic proxy in the Black Sea (Bahr et al., 2005, 2008; Kwiecien et al., 2008; Soulet et al., 2011a; Constantinescu et al., 2015). Original MD04-2790 age-depth model was performed until to the depth 1990 cmbsf (31.3 ka), corresponding to depth 1595 cmbsf in core GAS-CS01. Below, MD04-2790 LST record did not provide reliable tie-point compared to Hulu Cave record (Soulet et al., 2011a). Hence, below the depth 1990 cmbsf in MD04-2790 and the depth 1595 cmbsf in GAS-CS01, the chronology is based on radiocarbon dates (*Dreissena* sp. and bulk organic matter; Table 2). We implemented these chronological constraints (Supplementary Tables S1 and S2) in Oxcal (Bronk Ramsey, 2001, 2017, 2008; 2009; Bronk Ramsey and Lee, 2013).

As reservoir ages are unconstrained for this period, we applied a vague reservoir age correction following a uniform distribution spanning 0 to 5000  $^{14}\text{C}$  yrs correction. Oxcal codes and further details of the modelled age-depth models are available in Supplementary Online Material. We found that the base of both cores consistently dates back to ~33.5 ka (Supplementary Figs. S1 and S2).

## 6. Results

### 6.1. GAS-CS01 lithology

The analysis of core GAS-CS01 shows the classic regional lithological succession consisting of the microlaminated coccolith ooze (MCO; 0–0.04 mbsf), the black-brown micro-laminated sapropel (0.04–0.52 mbsf), and the carbonate-rich layers (down to 2.53 mbsf) overlying the Red Layers (2.53–4.26 mbsf). Below the Red Layers down to the bottom (32.1 mbsf), the GAS-CS01 lithology consists of even, parallel clastic rhythmites. This lithological succession, found from the north-west Black Sea upper slope (Bahr et al., 2005; Major et al., 2002; Soulet et al., 2011a) to the Danube deep-sea fan (Constantinescu et al., 2015), corresponds to 'marine' Unit I (MCO,  $<2720 \pm 160$  cal a BP) and Unit II (sapropel, deposited from  $8080 \pm 250$  cal a BP) and below, 'lacustrine' Unit III (glacial 'banded lutites') described by Ross and Degens (1974). Consequently, the carbonate-rich silty clay is interpreted as the upper part of the 'lacustrine' Unit III (Dean and Arthur, 2011). This sediment deposited during the late glacial (including the Bølling-



Allerød Interstadial and the Younger Dryas cold event), from  $15.7 \pm 0.3$  cal ka BP (upper part of the Red Layers; Soulet et al., 2011a) and the Initial Marine Inflow ca. 9 ka (Soulet et al., 2011b). Based on the above, core GAS-CS01 therefore consists of a very high-resolution record of the glacial (*sensu stricto*, > 16 ka) 'lacustrine' Unit III (until ca. 33.5 ka; see Part 5 'Age-depth model').

In detail, the glacial sequence of GAS-CS01 is fully laminated (total of 3815 laminae/beds revealed by X-ray imagery) and consists of even, parallel clastic rhythmites that resemble the varve pattern of Degens et al. (1978). They consist of silty to sandy graded deposits, evolving gradually from millimetre- (*i.e.* laminae; Scandinavian-type lacustrine varves of Degens et al., 1978) to decimetre-thick deposits (*i.e.* beds; megavarves of Degens et al., 1978) from the Red Layers (2.53–4.26 mbsf) to the core bottom (32.1 mbsf) (Figs. 4 and 6). They are separated by muddy intervals of similar thickness (*i.e.* mm-to dm-thick from top to bottom). Interestingly, the grain-size of the deposits is positively correlated with the thickness of the clastic intervals, from silt-sized grains in the Red Layers to sand-sized particles in the deeper part of GAS-CS01. High-resolution grain-size analyses reveal the superposition of (basal) coarsening-

up and (top) fining-up sequences throughout GAS-CS01. This pattern is mirrored by the millimetre-scale XRF Zr/Rb, well-known as a semi-quantitative grain-size indicator (Dypvik and Harris, 2001) (Figs. 7–9). All these results (and the inversely graded facies in particular) suggest that the clastic rhythmites in GAS-CS01 are hyperpycnite sequences, *i.e.* deposits that are related to quasi-steady hyperpycnal (*i.e.* 'above a density threshold') turbidity currents (Mulder et al., 2003; Mulder and Alexander, 2001). The detailed observation of X-ray images and thin-sections reveal similar sedimentary deposits (including 4841 laminae) at site MD04-2790 (Soulet et al., 2011a), ~20 km east of GAS-CS01. This highlights the regional imprint of hyperpycnal flows in the north-west Black Sea 'Lake' during the last glacial period.

## 6.2. Hyperpycnal turbidites frequency

The frequency of hyperpycnal turbidite deposits (hyp.250 yr<sup>-1</sup>) has been estimated for cores GAS-CS01 and MD04-2790 (Fig. 10b and Supplementary Online Material). The two cores present similar trends. A peak in hyperpycnal turbidite frequency (>100 hyp.250

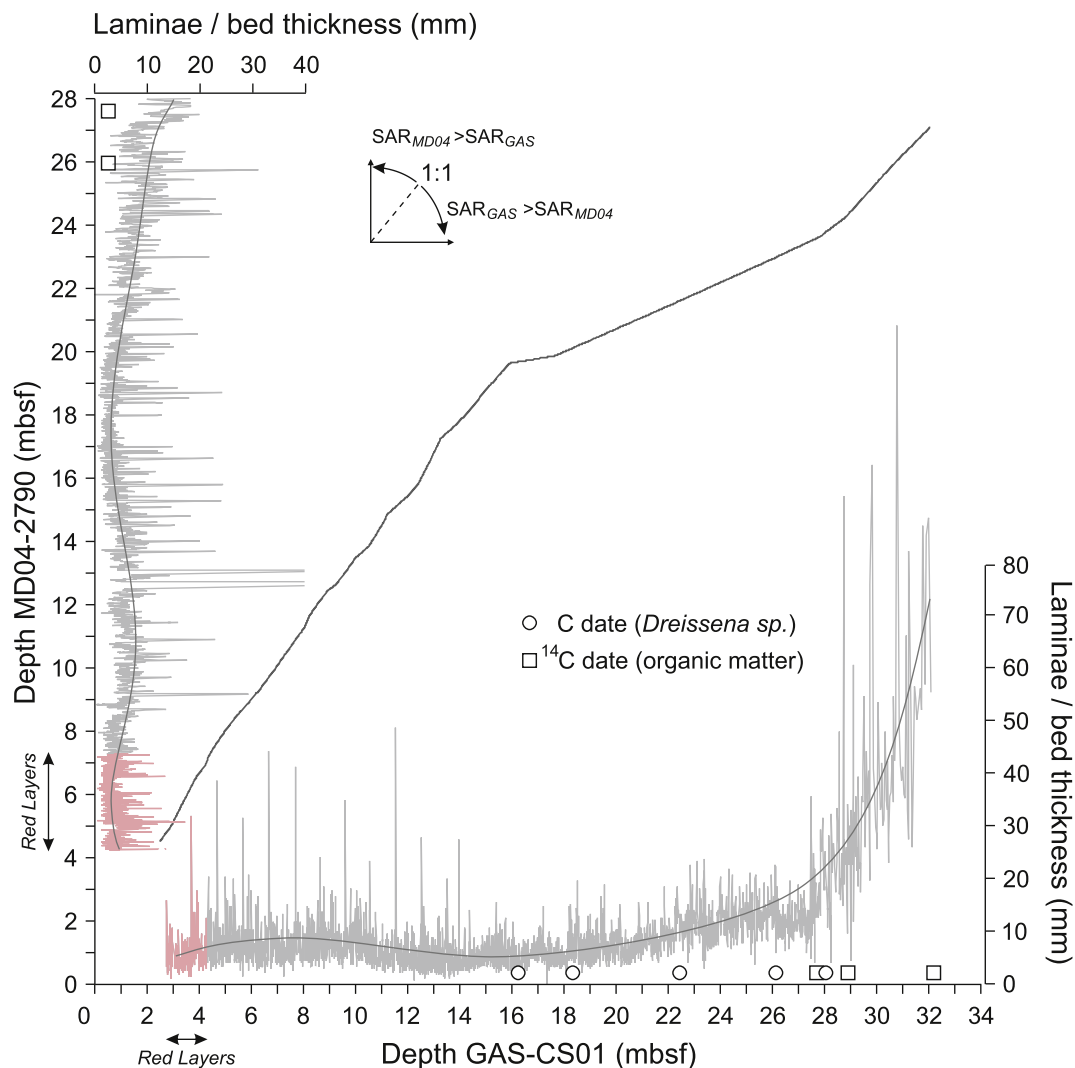


**Fig. 6.** Depth-depth relationship between cores GAS-CS01 and MD04-2790 based on the stratigraphic correlations shown in Fig. 5. See section 5 'Age-depth model' and Supplementary Online Material for details, and Table 2 for the radiocarbon dates. The laminae/bed thickness and the Red Layers interval are also shown. Note that sediment accumulation rates (SAR) at site GAS-CS01 are significantly higher than at site MD04-2790 before ca. 31 ka (*i.e.* below depth 1595 mbsf in core GAS-CS01 and depth 1990 mbsf in MD04-2790), consistent with the significant thickness difference of hyperpycnal beds observed at the two sites on the same time interval. The decimeter-scale hyperpycnite beds recognized in the lower part of core GAS-CS01 are detailed in Fig. 7. (For interpretation of the references to color in this figure legend, the reader is referred to the Web version of this article.)

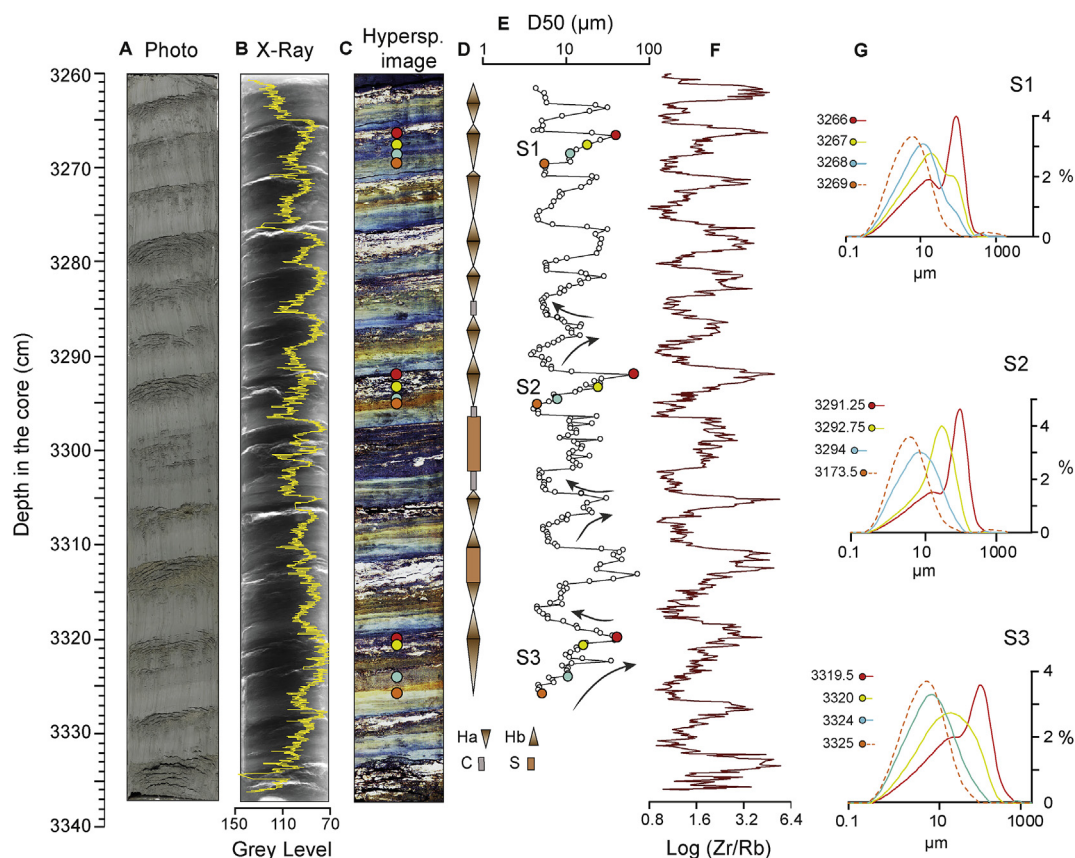


**Fig. 7.** High-resolution analysis of the pluricentimeter-thick clastic rhythmites, interpreted as hyperpycnites (H), observed in the basal part of core GAS-CS01 (>28.5 mbsf; here Section 34/34, 3139–3214 cmbsf; ca. 33 ka). a, Digital photograph; b, X-ray image and grey-level measurements (yellow line); c, Hyperspectral image highlighting changes in the sediment texture and/or composition. Colored circles refer to the grain-size analyses shown in e and g (sedimentary sequences S1, S2 and S3); d, Schematic lithological succession based on grain-size (e) and XRF (f) measurements. Ha and Hb correspond to the (basal) coarsening-up (i.e. waxing period of river discharge) and (top) fining-up (i.e. waning period of discharge) sequences of the hyperpycnites (Mulder et al., 2003) respectively. C: clay. S: silt-sand. e, Grain-size measurements (median or D50, i.e. grain-size -  $\mu\text{m}$ - at which 50% of sample is finer). Mean sampling resolution of 0.25 cm ( $n = 218$ ). Black arrows highlight some representative coarsening-up and fining-up sequences. Colored circles refer to the grain-size analyses shown in c and g; f, XRF Zr/Rb ratio, here used as a semi-quantitative grain-size indicator (Dypvik and Harris, 2001); g, Particle size distribution of discrete sediment samples (colored circles in c and e) from the coarsening-up sequences S1, S2 and S3. (For interpretation of the references to color in this figure legend, the reader is referred to the Web version of this article.)

$\text{yr}^{-1}$ ) is observed from ca. 32.5–30.5 ka with a maximum (up to 380  $\text{hyp.250 yr}^{-1}$  at GAS-CS01) estimated at ca. 31 ka. A rapid decrease is observed thereafter (<50  $\text{hyp.250 yr}^{-1}$ ), followed by a new increase centred at 29–27.5 ka (~150  $\text{hyp.250 yr}^{-1}$  at MD04-2790). Then, a ~10-kyr-long period (from ca. 27 to 17 ka) of moderate hyperpycnal turbidite frequency fluctuating between ~15 and 50  $\text{hyp.250 yr}^{-1}$  is observed. During this interval, two main episodes of increasing frequency (up to ~50–70  $\text{hyp.250 yr}^{-1}$ ) are observed, at ca. 25.3–23.8 ka and at ca. 22.3–19 ka. A last peak in hyperpycnal turbidite frequency is observed at the two sites at 17.2–16 ka, i.e. during the deposition of the Red Layers. The evolution of sediment accumulation rates calculated for the two cores strictly follows that of the hyperpycnal turbidite frequency (Fig. 10c).

### 6.3. Sedimentary geochemistry

#### 6.3.1. Clay mineralogy

The GAS-CS01 clay mineralogy ( $n = 146$ ; Fig. 10d and e and Supplementary Online Material) reveals the dominance of both smectite ( $39 \pm 13\%$ ) and illite ( $36 \pm 10\%$ ) over chlorite ( $15 \pm 7\%$ ) and kaolinite ( $11 \pm 5\%$ ). From ca. 31 to 17.2 ka, the abundance of clay minerals fluctuates (up to ~15–20% variability for smectite) but is relatively stable in comparison to the >31 ka (peak in hyperpycnal

turbidite frequency; see Part 6.2) and <17.2 ka (Red Layers) intervals. Indeed, the oldest interval of GAS-CS01 is characterised by high abundances in illite (~40–45%) and chlorite (~20–30%), but low abundances in smectite (~30%) and kaolinite (~5–10%), in comparison to the subsequent ca. 31–17.2 ka interval. Similarly, the smectite content abruptly decreases from ca. 17.2 ka (<10%) while the content in kaolinite (up to 25%) and illite (up to 60–70%) significantly increases. Note that despite a general low abundance, kaolinite is the only clay mineral to show a distinct signature for the three time periods considered.

The Danube River tributary samples ( $n = 12$ ) were divided into three groups corresponding to the north-eastern Alps ( $n = 5$ ), the Carpathians ( $n = 5$ ) and the Dinarides ( $n = 2$ ) mountainous areas (Table 3). River samples from the Alps show an illite content of ~40–50% while chlorite represents ~25% of the clayey fractions. Kaolinite and smectite contents are low, usually <5%, except in the Iller River where the smectite content reaches 40%. Smectite (~55%) dominates over illite (~25–30%) in the Carpathians, while an inverse pattern is observed in the Dinarides (~45–50% and ~20–25% of illite and smectite, respectively). The clay mineralogy of these zones contrasts with that of the north-eastern Alps with significant abundance of kaolinite (~10–20%) and very low content of dolomite (<2%). Dolomite abundance is significant (up to 17%) in the Alpine



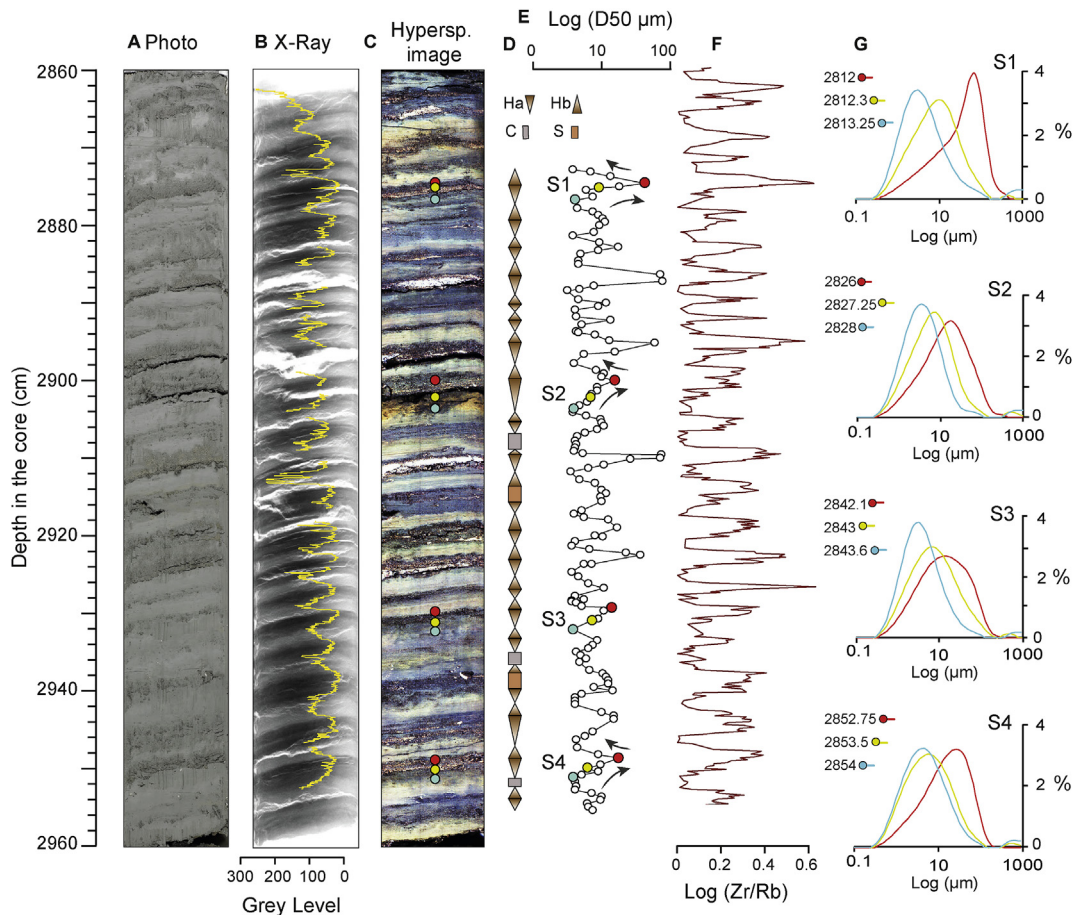


**Fig. 8.** High-resolution analysis of the centimeter-thick clastic rhythmites, interpreted as hyperpycnites (H), observed in the lower part of core GAS-CS01 (from ~22 to 28.5 mbsf; here Section 30/34, 2804–2859 cmbsf; ca. 32 ka). a, Digital photograph; b, X-ray image and grey-level measurements (yellow line); c, Hyperspectral image highlighting changes in the sediment texture and/or composition. Colored circles refer to the grain-size analyses shown in e and g (sedimentary sequences S1, S2, S3 and S4); d, Schematic lithological succession based on grain-size (e) and XRF (f) measurements. Ha and Hb correspond to the (basal) coarsening-up (i.e. waxing period of river discharge) and (top) fining-up (i.e. waning period of discharge) sequences of the hyperpycnites (Mulder et al., 2003), respectively. C: clay; S: silt-sand; e, Grain-size measurements (median or D50, i.e. grain-size  $\mu\text{m}$ - at which 50% of sample is finer). Mean sampling resolution of 0.25 cm ( $n = 149$ ). Black arrows highlight some representative coarsening-up and fining-up sequences. Colored circles refer to the grain-size analyses shown in c and g; f, XRF Zr/Rb ratio, here used as a semi-quantitative grain-size indicator (Dypvik and Harris, 2001); g, Particle size distribution of discrete sediment samples (colored circles in c and e) from the coarsening-up sequences S1, S2 and S3. (For interpretation of the references to color in this figure legend, the reader is referred to the Web version of this article.)

ivers.

### 6.3.2. Illite crystallinity index

The illite crystallinity index (ICr) in GAS-CS01 ( $n = 146$ ) shows values ranging from  $\sim 0.25^\circ$  at the core bottom to  $\sim 0.60^\circ$  in the Red Layers interval (Fig. 10f and Supplementary Online Material). In between, the ICr values range from  $\sim 0.30^\circ$  to  $0.40^\circ$ . The increase in ICr values in the Red Layers is abrupt (at ca. 17.2 ka). In contrast, the ICr decreases gradually from ca. 33.5 ka to ca. 30 ka.

The ICr values of the Danube tributary river samples ( $n = 12$ ) are more homogeneous than in core GAS-CS01. ICr values reach a maximum of only  $0.34\text{--}0.39^\circ$  in the northern Alps (Iller River and the Danube at Passau). The ICr minimum ( $0.20^\circ$ ) is found in the (upper) Drava River sample, eastern Alps (Table 3).

### 6.3.3. $\epsilon_{\text{Nd}}$

The  $\epsilon_{\text{Nd}}$  dataset used in this study is from core MD04-2790 ( $n = 84$ ) for the ca. 28–10 ka period (Soulet et al., 2013) and from core GAS-CS01 ( $n = 14$ ) for the ca. 32–28 ka period (Fig. 10g). GAS-CS01 sediment show an  $\epsilon_{\text{Nd}}$  value of  $-11.0$  at ca. 28 ka, in line with the  $\epsilon_{\text{Nd}}$  signature of  $-11.3 \pm 0.3$  ( $n = 53$ ) for the glacial MD04-2790 sediment (except Red Layers, see the discussion below).  $\epsilon_{\text{Nd}}$  values

gradually change towards the core bottom, reaching about  $-9.4 \pm 0.1$  ( $n = 9$ ) over the ca. 33.5–31 ka period (Supplementary Online Material).

## 7. Discussion

### 7.1. Linking GAS-CS01 and MD04-2790 sedimentary sequences to Central European rivers

#### 7.1.1. Sedimentological evidence for direct connection between Central European sediment sources and Black Sea depositional sinks

The sedimentological investigation of core GAS-CS01 shows that the continuous, rhythmic layering observed throughout the core (Fig. 4) consists in the succession of coarsening-upward and fining-upward units characteristics of hyperpycnal turbidity-current deposits (i.e. hyperpycnites; Mulder et al., 2003), at both the decimetre (lower part of GAS-CS01; Fig. 7) and millimetre scales (upper part of the core; Fig. 9). Thus, we attribute each clastic rhythmite (laminae or beds; Fig. 4) in GAS-CS01 to a discrete hyperpycnal flow. Hyperpycnal flows are defined as a bottom-riding flow evolving from a hyperpycnal plume, which descends to the basin floor as a result of excess density generated by its sediment load.

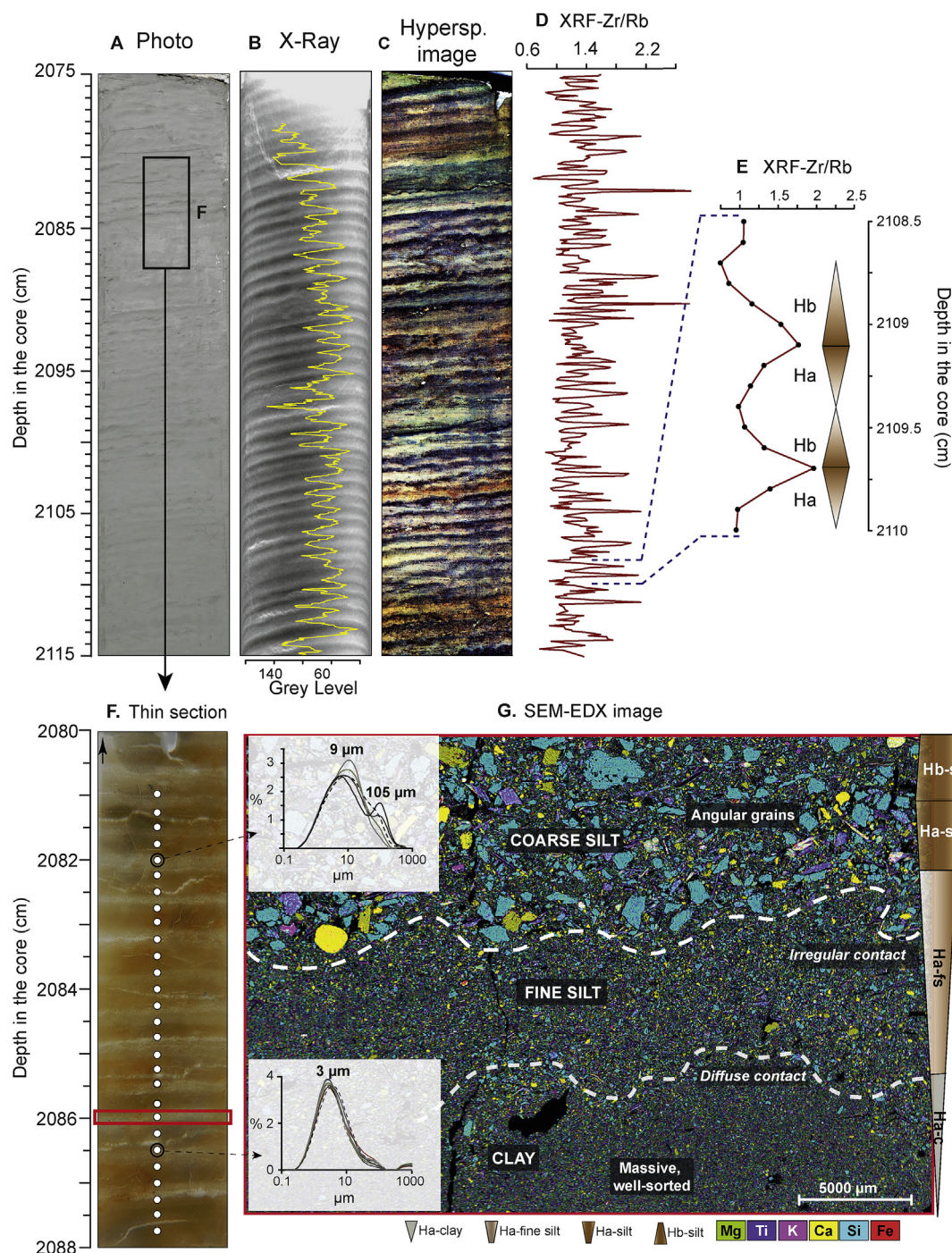
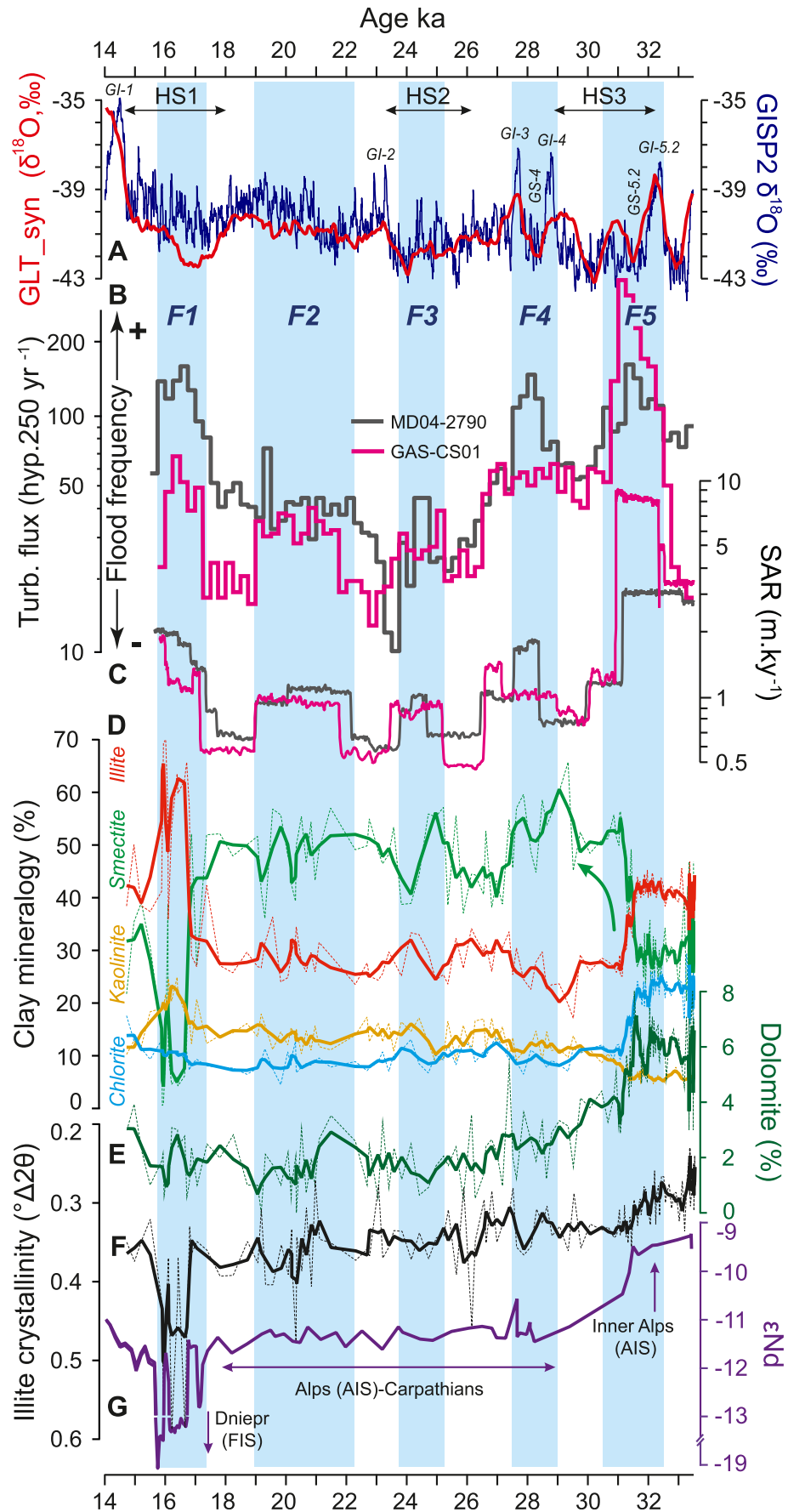


**Fig. 9.** High-resolution analysis of the subcentimeter-thick clastic rhythmites, interpreted as hyperpycnites (H), observed in core GAS-CS01 (down to ~22 mbsf; here Section 22/34, 2031–2083 cmbsf; ca. 31 ka). a, Digital photograph; b, X-ray image and grey-level measurements (yellow line); c, Hyperspectral image highlighting changes in the sediment texture and/or composition; d, XRF Zr/Rb ratio, here used as a semi-quantitative grain-size indicator (Dypvik and Harris, 2001); e, Focus on the XRF Zr/Rb ratio. The Zr/Rb variability, similar to that observed for thicker clastic rhythmites in GAS-CS01 (Fig. 7 and 8), suggest coarsening-up and fining-up sequences; f, Thin section photograph (2039–2047.5 cmbsf) showing subcentimeter-thick clastic rhythmites. White circles refer to the grain-size analyses shown in g. Mean sampling resolution of 0.25 cm ( $n = 31$ ); g, SEM-EDX image of a coarsening-up sequences (see the red square in f for location). The colour variability highlights the sediment geochemistry (see the colour boxes). Coarse grains are mainly quartz (Si) and dolomite grains (Mg, Ca). Note their angular character. Particle size distribution (white boxes) for clayey ( $n = 9$ ) and silty ( $n = 5$ ) intervals are shown. A schematic lithological succession is proposed on the right. Ha and Hb according to Mulder et al. (2003). (For interpretation of the references to color in this figure legend, the reader is referred to the Web version of this article.)

Hyperpycnal flows are thus seen as the continuation of river discharges (i.e. floods) in subaqueous environments (Mulder et al., 2003, 1998; Mulder and Syvitski, 1995; Normark and Piper, 1991; Piper and Normark, 2009). They are frequent in freshwater lakes

where only small particle density thresholds are necessary to trigger plunging (Mulder et al., 2003). The brackish water conditions prevailing in the Black Sea during the last glacial period (Deuser, 1972; Marret et al., 2009; Ross et al., 1970; Schumilovskikh





et al., 2014; Soulet et al., 2010; Wegwerth et al., 2016), combined with the increased surface runoff and sediment load of the western Black Sea rivers (e.g. Danube, Dniepr) due to the combination of reduced vegetation cover and widespread permafrost (Kasse et al., 2010; Sidorchuk et al., 2011, 2008) likely favoured the generation of hyperpycnal flows and their deposits at the GAS-CS01 site. The recording of these events, and by extension of the river floods, was also favoured by the proximity to the GAS-CS01 site and the delta of the western Black Sea rivers. Indeed, the glacial lowstand conditions (lake level ~90–120 m below the present sea level; Figs. 1 and 2) significantly reduced the river mouth distance to the shelf margin. This evidence suggests that the 3815 hyperpycnites of core GAS-CS01 provides a high-resolution flood record in the north-west Black Sea over the ca. 33.5–15 ka interval. Similarities in both the stratigraphy (see the XRF  $\text{Ca}_{\text{norm}}$  for a prominent example; Fig. 5) and sedimentology (i.e. rhythmic layering throughout; Fig. 6) observed in core MD04-2790 (Soulet et al., 2011a), ~20 km east of GAS-CS01, highlights the regional imprint of river floods in the north-western part of the glacial Black Sea 'Lake'.

Reconstructed hyperpycnite frequency indicates that both GAS-CS01 and MD04-2790 sites experienced five main periods of increased flood frequency ( $F_x$ ), each of 1.5–3 kyr duration, over the ca. 33.5–15 ka interval. These periods occurred simultaneously at both sites, at ca. 32.5–30.5 ka ( $F_5$ ), corresponding to the peak maximum, and at ca. 29–27.5 ka ( $F_4$ ), ca. 25.3–23.8 ka ( $F_3$ ), ca. 22.3–19 ka ( $F_2$ ) and ca. 17.2–15.7 ka ( $F_1$ ) (Fig. 10b and c). The simultaneity of each of the  $F_x$  periods at sites GAS-CS01 and MD04-2790 importantly suggests a common forcing and, potentially, a unique river source at the two sites. This is fittingly demonstrated for the  $F_1$  period, ca. 17.2–15.7 ka. Geochemical investigations of MD04-2790 sediment and the use of neodymium isotopic composition show that the sediment composing the Red Layers originated from the decaying FIS and were transported to the Black Sea by the Dniepr River (Soulet et al., 2013). Thus, the  $F_1$  peak in GAS-CS01 and MD04-2790 result from the increase in the frequency of hyperpycnal flows generated at the Dniepr River mouth in response to ice mass fluctuations ~1200 km northward (Fig. 1; Soulet et al., 2013). The available geochemical dataset reveals that the unique, major river source for hyperpycnal flows over the ca. 33.5–17.2 ka interval and the  $F_2$ ,  $F_3$ ,  $F_4$  and  $F_5$  peaks was the Danube River (see Part 7.1.2). The concomitance between climate, sediment input and geochemical signature changes (smectite abundance,  $\epsilon_{\text{Nd}}$ , etc.; Fig. 10) excludes both an autogenic origin (i.e. internally generated 'noise') and lake-level changes (highly debated over the last glacial period; see Lericolais et al., 2011 and Vidal et al., 2010 for contrasting conclusions) for the observed variability in the sedimentary record at the GAS-CS01 and MD04-2790 sites (see Part 7.2).

### 7.1.2. Deciphering river sources

**7.1.2.1. Neodymium isotopic composition.** The sediment of the Red Layers deposited between ca. 17.2 and 15.7 ka ( $F_1$  peak) are characterised by  $\epsilon_{\text{Nd}}$  values of  $-14.5 \pm 1.3$  (down to  $-18$ ;  $n = 24$ ; Soulet et al., 2013). These values are close to  $\epsilon_{\text{Nd}}$  values of sediments of the Baltic area (Boswell et al., 2019, 2018; Soulet et al., 2013; Toucanne

et al., 2015) and the rivers Dniepr ( $\epsilon_{\text{Nd}}$  of  $-14$ ; Soulet et al., 2013) and Don ( $-14.3$ , this study) showing that the Red Layer sediments originated from the decaying FIS (Soulet et al., 2013). In contrast, the glacial sediment in MD04-2790, from ca. 28 ka (oldest  $\epsilon_{\text{Nd}}$  analysis in Soulet et al., 2013) to 11.7 ka shows homogenous but very distinct  $\epsilon_{\text{Nd}}$  values of  $-11.3 \pm 0.3$  ( $n = 53$ ). The latter signature is close to that of the European Alps (Soulet et al., 2013), for which the northern and eastern parts (sediment yield of 160 and 220 t km<sup>2</sup>.yr<sup>-1</sup>, respectively; Hinderer et al., 2013) represent a substantial contribution to the Danube sediment discharge (mean sediment yield: 83 t km<sup>2</sup>.yr<sup>-1</sup>). Indeed, Alpine rivers carry fine-grained sediments with modern  $\epsilon_{\text{Nd}}$  values ranging from about  $-10.8$  for the Pô River (southwestern Alps; Frost et al., 1986),  $-10.2 \pm 0.5$  for the Rhône River (western Alps; Henry et al., 1994) and  $-9$  for the Rhine (north-western Alps; Bayon et al., 2015) and the Danube (north-eastern Alps) rivers (Soulet et al., 2013). The Nd isotopic values of these Alpine rivers match those of the Quaternary loess of the Carpathian Basin ( $-10.4 \pm 0.6$ ,  $n = 20$ ; Újvári et al., 2012). Based on the above, we thus assume that the glacial  $\epsilon_{\text{Nd}}$  signatures of  $-11.3 \pm 0.3$  at site MD04-2790 are mainly ascribed to the Alps-Carpathian realm and, by extension, to the Danube River. Nevertheless, it cannot be ruled out that a slight contribution from the Dniepr and Don ( $\epsilon_{\text{Nd}}$  of about  $-14$ ) at the studied sites possibly lowered the 'pure'  $\epsilon_{\text{Nd}}$  signature ( $-11/-9$ ) of the Danube to its lower (i.e. unradiogenic) end members during the last glacial period. This mixing is supported by the significant increase in  $\epsilon_{\text{Nd}}$  at ca. 33–31 ka ( $F_5$  peak), with radiogenic values (about  $-9$ ) that undoubtedly excludes all river sources except that of the Danube at that time.

**7.1.2.2. Clay mineralogy and illite crystallinity.** Illite and smectite dominates the clay mineralogy of GAS-CS01 sediment (Fig. 10d). Illite is a good marker for northern river sources in the Black Sea (Stoffers and Müller, 1978; Tudryn et al., 2016), including the Danube River (Table 3), but it shows a maximal abundance (>40%) both during the 'non-radiogenic' Dniepr-sourced  $F_1$  peak (i.e. Red Layers;  $\epsilon_{\text{Nd}}$  down to  $-18$ ) and the 'radiogenic' Danube-sourced  $F_5$  peak ( $\epsilon_{\text{Nd}}$  about  $-9$ ). Thus, it cannot be used to decipher sediment sources in the north-west Black Sea. The combination of illite with kaolinite at GAS-CS01 during the  $F_5$  peak is a peculiar mineralogical signature over the studied interval. Illite and kaolinite are typical of (paleo)soils, pedogenic processes and long-term weathering of sedimentary basins (Chamley, 1989) and appear as the main clay minerals in the Volga and Dniepr-Donets basins (Makshaev and Svitoch, 2016; Misch et al., 2018; Vishnevskaya and Sedaeva, 2000), thus supporting an eastern Central European origin for the deposition of Red Layers (Soulet et al., 2013). On the other hand, the low kaolinite content (~5–15%), together with the  $\epsilon_{\text{Nd}}$  values, exclude this source (at least as a major contributor) for glacial sediment input to the margin between ca. 33.5 and 17.2 ka.

Smectite content is low to absent in the Red Layers but represents 30–60% of the ca. 33.5–17.2 ka interval at GAS-CS01. Smectite is well-represented in the Danube drainage basin (Tudryn et al., 2016), particularly in the Dinarides (~20–25%) and the Carpathians (~45–55%; Table 3). In the latter region, it probably

**Fig. 10.** a,  $\delta^{18}\text{O}$  from GISP2 on the GICC05 timescale and the INTIMATE event stratigraphy. Greenland Stadials (GS) and Greenland Interstadials (GI) are the Greenland expressions of the characteristic Dansgaard-Oeschger events that represent cold and warm phases of the North Atlantic region, respectively (Rasmussen et al., 2014). The Greenland synthetic  $\delta^{18}\text{O}$  record (GLT<sub>syn</sub>) of Barker et al. (2011), placed on the absolutely dated Chinese speleothem record (Hulu Cave on this time interval), is also shown; b, c, Flood frequency and sediment accumulation rates (SAR) off the Danube River, respectively; d, e, f, Clay mineralogy, dolomite abundance and illite crystallinity (three-points average) at core GAS-CS01, respectively. The green arrow highlights the increase in smectite content to higher values, interpreted as the signature of the western Molasse Basin and Rhine glacier in response to the rapid growth of the AIS (see Fig. 11 for details); g, Neodymium isotopic composition (expressed in  $\epsilon_{\text{Nd}}$ ) in core MD04-2790 (ca. 28–10 ka; Soulet et al., 2013) and GAS-CS01 (ca. 33.5–28 ka; this study) as a proxy for sediment provenance. The vertical light blue bars highlight the timing for the  $F_5$  (ca. 32.5–30.5 ka),  $F_4$  (ca. 29–27.5 ka),  $F_3$  (ca. 25.3–23.8 ka),  $F_2$  (ca. 22.3–19 ka) and  $F_1$  (ca. 17.2–15.7 ka) peaks -based on both the flood frequency (b) and the SAR (c)- interpreted as periods of enhanced flux of sediment-laden meltwater on the north-west Black Sea margin. HS refers to Heinrich Stadials. (For interpretation of the references to color in this figure legend, the reader is referred to the Web version of this article.)

originates from chemical hydrothermal weathering of volcanic rocks (Chamley, 1989), as shown in the Tisza basin (e.g. Tokaj Mountains and the Calimani-Gurghiu-Hargita volcanic chain in the northern and eastern Carpathians, respectively; Bobos, 2012; Kiss et al., 2010). In the Alpine domain of the Danube, smectite is restricted to the western part of the Molasse Basin as shown by mineralogical data from the Iller River (40%; Table 3) and the neighbouring Lake Constance (Müller and Quakernaat, 1969). It is important to note that the Rhine glacier covered Lake Constance during the last glacial period and drained into the Danube (Ellwanger et al., 2011), thus providing a significant source of Alpine smectite, with chlorite and dolomite (Müller and Quakernaat, 1969; Schmieder et al., 2004), to the north-west Black Sea. Chlorite content is also significant (~25–30%) in the Alpine domain, in rivers draining both the northern (e.g. Inn, Enns) and central eastern Alps (i.e. eastern Dolomites and the Drava River; Table 3), where physical weathering at high altitudes dominates (Chamley, 1989; Müller and Quakernaat, 1969). Chlorite content in GAS-CS01 reaches a maximum (~25%) during the F<sub>5</sub> peak together with an increase in dolomite (~10%), a common mineral in the inner Alps (Upper Rhine, Iller, Enns, Drava; Table 3). Thus, the mineralogical signature for the F<sub>5</sub> peak suggests a significant Alpine contribution. More generally, these data together with  $\epsilon_{\text{Nd}}$  support our contention that the Danube River was the main source for sediment input to the margin over the ca. 33.5–17.2 ka interval.

This is further supported by the ICr values of  $0.32 \pm 0.04$  at GAS-CS01 (Fig. 10f) that fit well with those obtained for the Danube river samples ( $0.3 \pm 0.05$ ; Table 3). Such values are indicative of illite formation in low-grade metamorphic, high anchizonal conditions (i.e. lower greenschist facies; Kubler, 1967), typical of the central and eastern Alps (Bousquet et al., 2008; Krumm et al., 1988; Rantitsch, 1997; Schramm, 1991), the Dinarides (Rainer et al., 2002) and the Carpathians (Árkai, 1991; Árkai et al., 2003; Ciulavu et al., 2008). Interestingly, the F<sub>5</sub> peak shows ICr values down to  $0.23^\circ$  pointing to anchizonal-epizonal thermal conditions (i.e. blueschist facies). Such metamorphic conditions are restricted to the western (Gemer and Bükk units; Árkai, 1991) and southern parts (Danubian window; Ciulavu et al., 2008) of the Carpathians, and the Engadine (up to 4049 m at Piz Bernina) and Tauern (up to 3898 m at Grossglockner) windows of the eastern and central Alps, respectively (Bousquet et al., 2008; Nievergelt et al., 1996; Schramm, 1991) (Figs. 1 and 3). The dolomite enrichment at ca. 33–31 ka together with the above ICr values, points to these high alpine sources for the F<sub>5</sub> peak sediments, and by extension to the Drava (and its tributaries; e.g. Mur), that drain both the Dolomites and the southern Tauern window, and the Inn rivers. The Inn River has its source in the Bergell Massif (upper Engadine valley) and the Salzach River, its main tributary, drained the northern part of the Tauern window (Fig. 3). Interestingly, the  $\epsilon_{\text{Nd}}$  values of the F<sub>5</sub> peak ( $-9.4 \pm 0.1$ ,  $n = 9$ ) match with the lower range of  $\epsilon_{\text{Nd}}$  values ( $-8.0 \pm 1.4$ ,  $n = 9$ ) determined for recent granites in the high Central Alps, including the Bergell Massif (Juteau et al., 1986). Altogether, the neodymium isotopic composition, the clay mineralogy and the ICr highlight the imprint of the Danube River on the north-west Black Sea margin sedimentation during the ca. 33.5–17.2 ka interval.

The above finding is in line with geomorphological aspects from the continent interior to the deep Black Sea. First, the modern contribution of the 'mountainous' Danube to the Black Sea exceeds that of the 'lowlands' Dniester, Dnieper and Don by a factor 8 (see Part 2.1; Milliman and Farnsworth, 2013; Milliman and Syvitski, 1992; Panin and Jipa, 2002), and this difference was strongly enhanced during the last glacial period by the presence of the AIS and Carpathian glaciers in the Danube drainage area (see Part 2.2). In contrast, the southern limb of the FIS entered the Upper Dniepr

basin only during a short period ca. 20–17 ka (Hughes et al., 2016; Karabanov and Matveyev, 2011; Soulet et al., 2013) (Fig. 1). Moreover, the physiography of the shelf-penetrating Danube Canyon (Popescu et al., 2004) and the high sediment inputs into the Danube deep-sea fan (Constantinescu et al., 2015) are indicative of both a high Danube sediment discharge and of a good connectivity between the Danube delta and the shelf margin where cores GAS-CS01 and MD04-2790 are located (Fig. 2). As such, the physiography of the margin suggests that the GAS-CS01 site was located at only ~20–30 km (~50 km for MD04-2790) from the Danube paleo-delta front (~130 km today) during glacial lowstand conditions (Popescu et al., 2004). Sediments deposited at sites GAS-CS01 and MD04-2790 between ca. 33.5 and 17.2 ka therefore record the evolution of the Danube basin.

## 7.2. From the Black Sea sedimentary record to the Alpine Ice Sheet

The above geochemical constraints, together with the timing for the F<sub>5</sub> (ca. 32.5–30.5 ka), F<sub>4</sub> (ca. 29–27.5 ka), F<sub>3</sub> (ca. 25.3–23.8 ka) and F<sub>2</sub> (ca. 22.3 to 19 ka) peaks, suggest increased Danube sediment discharges during Heinrich Stadial (HS; i.e. a stadial which contains a Heinrich event as defined by Sanchez Goñi and Harrison, 2010) 3 (ca. 32–29 ka), Greenland Stadial 4 (ca. 28.6–27.8 ka), HS 2 (ca. 26–23.5 ka) and during the period corresponding to the transition from the global LGM to the Northern Hemisphere deglaciation, respectively. This correlation highlights a close relationship between Danube River flood frequency and climate change. Nowadays, severe floods in the Alpine-Carpathian range are triggered by heavy, late spring to fall precipitation (e.g. Blöschl et al., 2013; Parajka et al., 2010). Holocene reconstructions of the flood frequency in the central and north-eastern Alps reveal centennial-to millennial-scale fluctuations in flood activity, with high flood activity correlated with cool periods (lows in solar activity, global/alpine glacier advances; Glur et al., 2013; Swierczynski et al., 2013; Wirth et al., 2013).

During the last glacial period, the continental ice build-up promoted cooling and enhanced aridity over Europe (Wu et al., 2007). Precipitation over the Alps and Carpathians occurred mainly in the form of snow. This inhibited the generation of floods from high-altitude sites, but participated in the build-up of glaciers over the Carpathians and of the AIS during the last glacial period (Figs. 1 and 3). The AIS built up, reached its glacial maximum extent (covering up to ~50,000 km<sup>2</sup> of the Danube watershed) and thickness (up to 2500 m in the Hohe Tauern region; Figs. 3 and 11), and eventually shrunk over the ca. 33–17.2 ka interval (e.g. Ivy-Ochs, 2015; Ivy-Ochs et al., 2008; Seguinot et al., 2018). Pullback of glaciers from their maximum extent (i.e. Alpine LGM) was underway by ca. 24–22 ka, and glaciers had receded within the mountain front by ca. 19–18 ka (e.g. Ivy-Ochs, 2015; Monegato et al., 2017; Reitner, 2007). This has been widely documented in the north-eastern Alps, including the Rhine, Iller, Isar, Loisach, Inn, Salzach, Enns and Drava valleys (Ellwanger et al., 2011; Habbe and Rögner, 1989; Heiri et al., 2014; Ivy-Ochs et al., 2008; Preusser, 2004; Reitner, 2012; Spötl et al., 2013; Starnberger et al., 2009; Van Husen, 2004). Thus, glaciers retreat must have supplied meltwater and sediment to the Danube sediment routing system.

The timing for the Alpine (and Carpathian; Makos et al., 2018, 2013) deglaciation closely matches that of enhanced Danube river floods from ca. 22 to 19 ka (F<sub>2</sub> peak). This strongly suggests that the F<sub>2</sub> peak originated from the rapid downstream transport of glaciogenic sediments by AIS (and possibly Carpathian glaciers) meltwater, an assumption supported by the glaciogenic character of the lithic grains found in GAS-CS01 (Supplementary Fig. S3). Onshore ice retreat and concomitant offshore sediment pulse is a common feature of large-scale glaciated sediment routing systems (e.g.



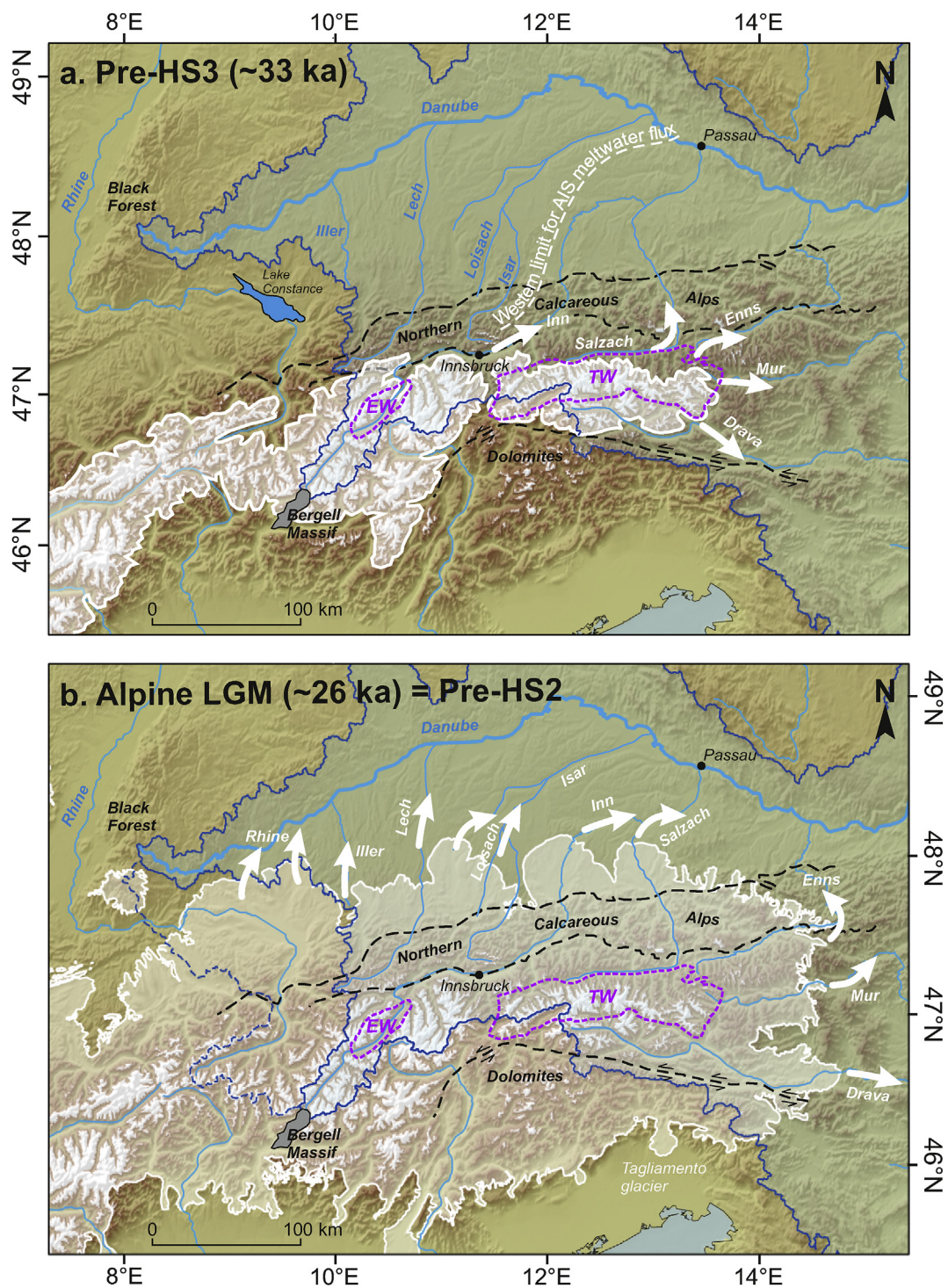


**Fig. 11.** Paleogeography of the central and eastern Alps, including the hydrographic network (blue lines) and glacial limits (white shaded areas) at (a) ca. 33 ka (i.e. before Heinrich Stadial 3 =  $F_5$  peak at the GAS-CS01 and MD04-2790 sites) and (b) during the local Last Glacial Maximum (LGM; Ehlers and Gibbard, 2004), ca. 26 ka (i.e. before Heinrich Stadial 2 =  $F_3$  peak). The proposed configuration at ca. 33 ka is based first on the geochemical evidences ( $ICR_{eNd}$ ) found at GAS-CS01 for significant inputs of terrigenous material from the Engadine (EW) and Tauern (TW) windows (purple dashed lines; via the Inn, Salzach, Enns, Mur and Drava rivers) into the north-west Black Sea ca. 32.5–30.5 ka (i.e. during the  $F_5$  peak interpreted as AIS melting; see the main text for details); and second, on the low content of smectite at the GAS-CS01 site before ca. 30.5 ka (and until ca. 33.5 ka at least; Fig. 10d). The smectite in the Alpine domain being restricted to the western part of the Molasse Basin (e.g. Iller River; Table 3) and the upper Rhine (Müller and Quakernaat, 1969), the clay mineralogy at GAS-CS01 suggests that these areas were mainly free of ice at ca. 33 ka (and until ca. 30.5 ka) as shown in (a). Such an ice configuration (with the Iller, Lech and Isar/Loisach rivers not connected to the AIS) is found using an equilibrium line altitude at ~2300 m above sea level (white, high-altitude areas; also shown in (b) for comparison). Note that the invasion of the northern Alpine foreland by the major AIS ice-streams (Alpine LGM) strongly modified the glacial hydrographic pattern of the Alpine Danube. Smectite content at GAS-CS01 suggests that the AIS growth (including the Iller glacier; Habbe and Rögnér, 1989) and the subsequent re-routing of the Rhine glacier meltwaters to the Danube (Ellwanger et al., 2011) occurred from ca. 30.5 ka. The white arrows show the main sources for AIS meltwater to the Danube. HS refers to Heinrich Stadials. (For interpretation of the references to color in this figure legend, the reader is referred to the Web version of this article.)

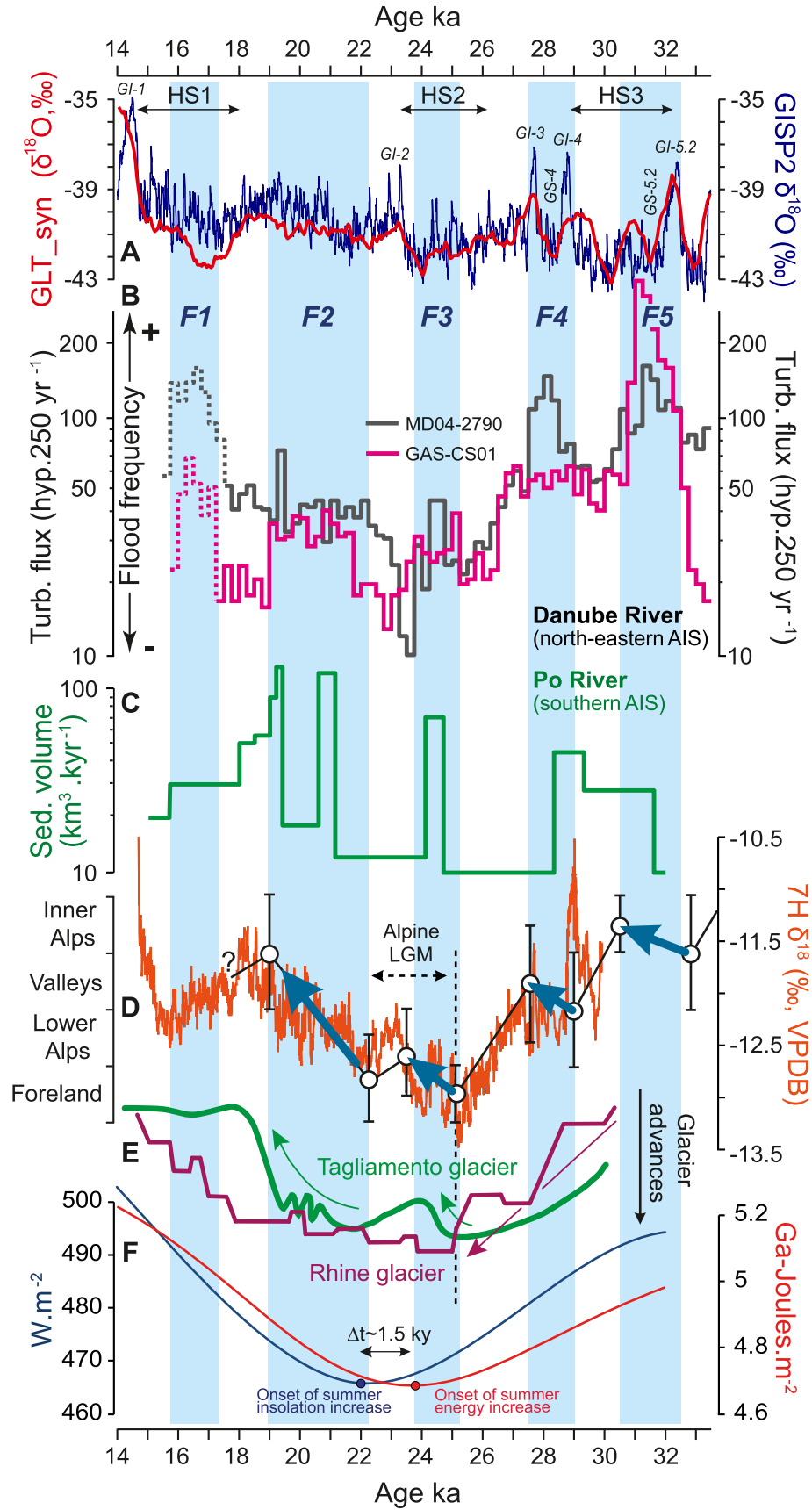


**Fig. 12.** a,  $\delta^{18}\text{O}$  from GISP2 (Rasmussen et al., 2014) and the GLT\_syn record (Barker et al., 2011). See Fig. 10a for details; b, Flood frequency of the Danube River (Fig. 10b). The dashed lines (between ca. 17.2 and 15.7 ka) correspond to the Dniepr River flood (Red Layers; Soulet et al., 2013); c, Sediment volume of the Po River lowstand wedge, based on seismic reflection data and the PRAD1-2 borehole (Fig. 1; Pellegrini et al., 2017, 2018); d, Ice-mass balance of the north-east AIS based on the Danube sediment records (open circles and

Mississippi in North America, Kolla and Perlmutter, 1993; Channel River, Rhine, Rhone or Po in Europe, Bonneau et al., 2017; Hinderer, 2001; Pellegrini et al., 2017; Toucanne et al., 2010). In these systems, sediment production greatly exceeds transport capacity, hence downstream release of sediments occurs through pulses of meltwater floods when glaciers retreat. Thus, the  $F_2$  peak (sourced by the AIS-Danube system) as well as the  $F_1$  peak (sourced by the FIS-Dniepr system; Soulet et al., 2013) share the common genetic origin of ice melting. Together with the geochemical results, we thus suggest that the  $F_5$  (ca. 32.5–30.5 ka),  $F_4$  (ca. 29–27.5 ka) and  $F_3$  (ca. 25.3–23.8 ka) peaks, just like  $F_2$ , were triggered by significant ice melting and meltwater production in the Danube basin.

Little is known about ice fluctuation in the Alps before the deglaciation (e.g. Ivy-Ochs et al., 2008). The Tagliamento end moraine system of the south-eastern Alps (Fig. 3) provides insights into AIS fluctuations at the LGM. Two phases of glacial culmination occurred from 26.5 ka and at ca. 23–21 ka, separated by a distinct recession which ended no later than ca. 23 ka (Monegato et al., 2017) (Fig. 12e). This recession, also recognized in the neighbouring Brenta glacier region (Rossato and Mozzi, 2016, Fig. 3), is concomitant with enhanced Danube river floods and the  $F_3$  peak, while the two glacier advances are coeval with the minima in the Danube River discharge at ca. 27–25.3 ka and from ca. 23.8 ka (Fig. 12b). The Tagliamento and Brenta glaciers were draining south into the Adriatic, suggesting that the timing of ice fluctuations in the Danube basin was similar to that of the south-eastern Alps with a significant melting episode at ca. 25.3–23.8 ka ( $F_3$  peak). The hypothesis is supported by the fact that both the Tagliamento and Brenta glaciers in the south-eastern Alps, and the Inn, Salzach, Traun, Mur and Drava glaciers in the Danube basin were all draining the Hohe Tauern region and the Engadine ice dome in the central eastern Alps (Florineth and Schlüchter, 2000; Seguinot et al., 2018, Fig. 3). Geochemical data characterizing the GAS-CS01 sediment during  $F_5$  peak (high  $\epsilon_{Nd}$  and dolomite content, and low ICr; see Part 7.1 and Fig. 10) also suggest this region as the source of sediment.

$F_5$  peak in hyperpynal flow frequency suggests a significant retreat of the AIS at ca. 32.5–30.5 ka, with significant remobilization (via meltwater) of the glacialic sediment from the Engadine (e.g. upper Inn) and Tauern (e.g. upper Salzach and Drava) valleys. By extension, this indicates that ice caps were mainly restricted to the high Central Alps before ca. 32 ka, with a configuration that could resemble that proposed in Fig. 11. This is consistent with the radiocarbon chronology of the Inn Valley that indicates that glaciers were upstream of (but close to) the Innsbruck region (i.e. ~100 km of the Alpine foreland) ca. 33–32 ka (Spötl et al., 2013). It is noteworthy that the sediment flux at the GAS-CS01 and MD04-2790 sites was greater during the  $F_5$  peak than during the  $F_2$ ,  $F_3$ , and  $F_4$  peaks. The amplitude of the  $F_5$  peak could be explained by very low lake-level conditions, basinward migration of the Danube delta or even lateral changes in sediment dispersal and depocenter considering the fact that the  $F_5$  peak is higher at site GAS-CS01 than at site MD04-2790 (Fig. 10). However, these forcings alone cannot explain the alpine geochemical signature (i.e. high Central Alps) observed at that time. As a result, we propose that the  $F_5$  peak (as well as the  $F_4$  peak, see below) is the result of a short term glacier retreat event that occurred in the course of the longer term growing phase of the AIS toward its LGM extent. Resulting pulse in meltwater flood flushed a huge amount of glacialic material (i.e. no

longer available) accumulated in the high Alps since the previous glaciation (MIS 4 or even before; Ivy-Ochs et al., 2008; van Husen, 2000). In addition, our results suggest that the rapid ice growth that led to the invasion of the northern Alpine foreland by the major AIS ice-streams at the LGM started after ca. 30.5 ka, i.e. after the retreat interval mirrored by the  $F_5$  peak, and ended no later than ca. 25.3 ka (onset of the  $F_3$  peak). Such timing is consistent with that reported for the western Carpathians (Makos et al., 2018) and the northern foreland of the Swiss Alps (e.g. Rhine glacier; Preusser et al., 2011) (Fig. 12d). Finally, the  $F_4$  peak suggests that the LGM ice advance was interrupted (with glaciers melting in the north-eastern Alps) between ca. 29 and 27.5 ka. Our results imply that the ice front in the Inn Valley (Spötl et al., 2013) advanced to its LGM position at a rate of about 20–45 m/year (~100 km in a maximum of 2200–5200 years).

This rapid change in AIS volume and extent modified the regional pattern of erosion (e.g. Jiao et al., 2018), which may explain the mineralogical changes observed at the GAS-CS01 site after the  $F_5$  peak. This includes in particular the dominance of smectite in clay assemblages (Fig. 10d) and the disappearance of the signature (ICr,  $\epsilon_{Nd}$ ; Fig. 10f and g) of the Engadine and Tauern source areas. These two regions were rapidly covered by ice (>1 km in thickness) at the LGM; Florineth and Schlüchter, 2000) and the sediment-laden meltwater reaching the north-west Black Sea then mainly originated from the ice-streams located in the northern Alpine foreland, including those of the Rhine (Ellwanger et al., 2011) and the Iller valleys (Habbe and Rögner, 1989) that remobilize smectite-rich sediments (Müller and Quakernaat, 1969, Table 3) (Fig. 11).

It is striking how Danube River flood activity ca. 33–17 ka closely resembles that of the Po River, Italy (Fig. 12c). Indeed, the  $F_5$ ,  $F_4$ ,  $F_3$  and  $F_2$  Danube peaks are coeval with rapid increases in sediment flux (up to 200 km<sup>3</sup>/kyr) in the Po delta, which accumulated ~350 m of sediment from the southern AIS ca. 32–14 ka (Pellegrini et al., 2018, 2017). This result indicates that the sediment flux of the Danube and Po rivers was not controlled by basin base level changes (i.e. water-level fluctuations) because they evolved independently in the Mediterranean and Black Seas during glacial periods (Badertscher et al., 2011). Hence, AIS mass-balance changes must explain the similar sediment flux pattern observed offshore of the Po and Danube rivers during glacial times. The close resemblance between AIS fluctuations in the Danube catchment and the regional precipitation pattern (i.e. 7H  $\delta^{18}O$  record of the Sieben cave system; Luetscher et al., 2015), that partly controlled glacier mass balance (Fig. 12d), suggests that the AIS as a whole was responding to large-scale climate forcing.

### 7.3. Enhanced surface melting of the Alpine Ice Sheet during periods of North Atlantic cooling

In the above discussion, we have showed that the  $F_5$  (ca. 32.5–30.5 ka),  $F_4$  (ca. 29–27.5 ka),  $F_3$  (ca. 25.3–23.8 ka) and  $F_2$  (ca. 22.3 to 19 ka) peaks in hyperpynal flow frequency, resulting from increased Danube sediment discharges, likely resulted from enhanced surface melting of the AIS during HS 3 (ca. 32–29 ka), Greenland Stadial 4 (ca. 28.6–27.8 ka), HS 2 (ca. 26–23.5 ka) and the very end of the global LGM. The timing of these episodes of AIS melting has important implications, at regional to continental scales. The last episode of AIS melting recorded in this study (i.e.  $F_2$

black line) and the 7H  $\delta^{18}O$  record from the Sieben Hengste cave system, Switzerland (Fig. 1 and 3; Luetscher et al., 2015). Thick blue arrows highlight AIS melting intervals, meltwater production and sediment-laden meltwater inputs to the north-west Black Sea margin (b); d, Fluctuations of the Rhine (purple; Preusser et al., 2011) and Tagliamento (green; Monegato et al., 2007) glaciers. Arrows highlight the glaciers fluctuations discussed in the main text; e, Summer energy (red line,  $\tau \sim 400$ ) (Huybers, 2006) and 21 June–20 July insolation for 45°N (blue line; Laskar et al., 2004). The vertical light blue bars highlight the timing for the  $F_5$  (ca. 32.5–30.5 ka),  $F_4$  (ca. 29–27.5 ka),  $F_3$  (ca. 25.3–23.8 ka),  $F_2$  (ca. 22.3–19 ka) and  $F_1$  (ca. 17.2–15.7 ka) flood events. HS refers to Heinrich Stadials. (For interpretation of the references to color in this figure legend, the reader is referred to the Web version of this article.)



peak in the Danube record, and its equivalent in the Po delta) occurred ca. 22–19 ka. This time interval corresponds to the onset of the widespread retreat of the Northern Hemisphere ice sheets in response to high northern latitude summer insolation forcing (Carlson and Clark, 2012; Clark et al., 2009). This event is well-documented for the FIS that rapidly retreated in the Baltic lowlands at that time (Hughes et al., 2016; Larsen et al., 2009; Stroeve et al., 2016; Toucanne et al., 2015, 2010). In contrast, the rapid acceleration in the FIS retreat from ca. 18 ka (HS 1; Hughes et al., 2016; Toucanne et al., 2015, 2010; Zaragosi et al., 2001) has no AIS equivalent in the north-west Danube and Po sedimentary records. Sediment flushed by AIS fluctuations younger than ca. 19 ka (i.e. Alpine Lateglacial, including the Gschnitz stadial ca. 17–16 ka; Ivy-Ochs, 2015) could have been trapped in glacier-shaped lake basins that formed during deglaciation (Hinderer, 2001). This is consistent with the idea that glaciers receded back into the mountain front during the ca. 22–19 ka melting event, especially in the north-eastern Alps (Ivy-Ochs, 2015; Reitner, 2007; van Husen, 2000). By extension, this suggests that the HS 1 melting episode (ca. 18–16.5 ka; Toucanne et al., 2015), if it existed at all in the Alps (e.g. Ravazzi et al., 2014; Wirsig et al., 2016; Lehmann et al., 2020), impacted only a restricted area and volume of ice. This implies that the forcing that caused the initial retreat of the FIS at ca. 22–19 ka was important enough to cause a catastrophic collapse of the AIS. The rapid AIS collapse from ca. 22 ka was likely forced by the summer energy of Huybers (2006) that increase from 23.5 ka at 45°N and precede the summer insolation by 1.5 kyr (22 ka at 45°N; Laskar et al., 2004) (Fig. 12e). This suggests that summer energy is a better indicator of glacial variability than insolation intensity (Huybers, 2006), and confirms that the AIS was a highly dynamic ice-sheet (Seguinot et al., 2018).

AIS melting events during HS 3 and HS 2 in both the Danube and Po catchments (Fig. 12c) and the substantial FIS recession in the Baltic lowlands (Boswell et al., 2019; Hughes et al., 2016; Toucanne et al., 2015) are concomitant within age-model uncertainties. HS 3 and HS 2 in the North Atlantic correspond to cold air and sea-surface temperatures, widespread sea ice and increased iceberg calving and dispersal from surrounding marine-terminating ice margins (Bard et al., 2000; Barker et al., 2009). This is in contrast to the expectation that ice sheets should expand in colder climates and shrink in warmer climates, given constant precipitation. Considering that ablation of land-based ice in mid-latitudes occurs primarily during summer months (Oerlemans et al., 2001), the melting of both the AIS and the FIS during HS 3 and HS 2 (as well as during Greenland Stadial 4 for the AIS) requires a high seasonality in western Europe. High seasonality implies enhanced summertime melting, and thus rising summer temperature, despite severely cool winters and the rapid expansion of sea ice in the North Atlantic as previously discussed by Buizert et al. (2014) and Denton et al. (2005, 2010) for HS 1 and the Younger Dryas cold reversal. High-resolution climate simulations and proxy evidence, including the disintegration of Alps glaciers and the Scottish ice cap, support the occurrence of warm European summers during HS 1 (i.e. the so-called Gschnitz stadial in the Alps; Lehmann et al., 2020) and the Younger Dryas (Bromley et al., 2018; Schenk et al., 2018; Magyari et al., 2019). The atmospheric blocking of cold westerly winds over western Europe would be a key mechanism according to Schenk et al. (2018) and such a forcing would have prevailed during HSs of the last glacial period. A strong shift in atmospheric circulation in Europe and over the Alps during and around the LGM (Becker et al., 2016; Beghin et al., 2015; Florineth and Schlüchter, 2000; Ludwig et al., 2016), including millennial-scale climate changes (Luetscher et al., 2015; Monegato et al., 2017), partly support this assumption. Whatever the mechanism responsible for driving stadial decay of the AIS, our results, together with those

obtained for the FIS for the last (Toucanne et al., 2015) and penultimate glacial periods (Boswell et al., 2019), strengthens the idea that warm European summers are likely a recurring feature of North Atlantic stadials.

## 8. Conclusion

The GAS-CS01 and MD04-2790 glacial sedimentary sequences of the Black Sea 'Lake' provide a continuous high-resolution record of the Danube River discharge over the ca. 33–17 ka period. The main results, based on sedimentological, mineralogical and geochemical analysis, are the following:

1. The Danube sediment routing system produced hyperpycnal discharges into the north-west Black Sea throughout the study interval, and their deposits (i.e. hyperpycnites) at the GAS-CS01 and MD04-2790 sites provide a continuous, high-resolution paleoflood record of the Danube River at the end of the last glacial period (ca. 33–17 ka);
2. Four main periods of enhanced Danube flood frequency ( $F_x$ ), each of 1.5–3 kyr duration, are recorded at ca. 32.5–30.5 ka ( $F_5$ ), at ca. 29–27.5 ka ( $F_4$ ), at ca. 25.3–23.8 ka ( $F_3$ ) and at ca. 22.3–19 ka ( $F_2$ ). The sediment of the  $F_2$  period are typical of the Alpine foreland, whereas that deposited during the  $F_5$  period shows mineralogical and geochemical signatures typical of the inner Alps (i.e. Engadine and Tauern windows). This suggests that the Danube River activity over the ca. 33–17 ka interval provides a valuable record of paleoenvironmental changes in the European Alps, and by extension of the north-eastern AIS, from the second part of MIS 3 to the deglaciation;
3. Our data and continental morphostratigraphical evidence, suggest that the AIS volume has drastically decreased at ca. 19 ka (and as soon as ca. 22 ka) since no fluctuation of the AIS is recorded at the studied sites after this date. On the other hand, millennial-scale fluctuations of the north-eastern AIS are recorded before the deglacial 22–19 ka event ( $F_2$ ), with three significant melting episodes, able to remobilize glacial sediment to the Black Sea, at ca. 32.5–30.5 ka ( $F_5$ ), at ca. 29–27.5 ka ( $F_4$ ) and at ca. 25.3–23.8 ka ( $F_3$ ). Ice advance occurred between these periods and both the mineralogical and geochemical data suggest that the rapid AIS growth from the inner Alps to its LGM position started from ca. 30.5 ka and ended no later than ca. 25.3 ka;
4. The  $F_5$  (ca. 32.5–30.5 ka),  $F_4$  (ca. 29–27.5 ka) and  $F_3$  (ca. 25.3–23.8 ka) events indicates enhanced surface melting of the AIS during HS 3 (ca. 32–29 ka), Greenland Stadial 4 (ca. 28.6–27.8 ka) and HS 2 (ca. 26–23.5 ka) when severely cold winters and the rapid expansion of sea ice prevailed in the North Atlantic. This new finding is in line with those recently reported for the southern FIS and reinforces the emerging view that warm summers and hence strong seasonality are key climatic features of western Europe during North Atlantic stadials.

## Acknowledgments

The authors are very grateful to S. Ker, co-chief of the GHASS cruise; T. Dalle-Mulle, J. Gouriou, A. Roubi, M. Rovere and M. Simon for technical support; B. Martin and S. Zaragosi for the preparation of sediment thin sections; A. Trinquier for assistance on the Neptune MC-ICPMS; E. Pelleter for the acquisition of the X-ray EDS maps; N. Gayet for the acquisition of the SEM images; A. Banak, B. Dennielou, T. Gardes, G. Lericolais, A. Mena, R. Silva-Jacinto, A. Van Exem and C. Zavala for invaluable discussions at various stages of this work; A. Chalm for English improvements; and G. Monegato and two anonymous reviewers for their helpful comments, which

greatly improved the manuscript. Samples from river banks were collected in one expedition by L.G. and two successive fieldwork seasons by a team from ETH Zurich (the later reported in Freymond et al., 2017). Authors also thank the crew and scientific teams of the ASSEMBLAGE (R/V Marion Dufresne) and GHASS (R/V Pourquoi Pas?) cruises for the recovery of the long-piston cores MD04-2790 and GAS-CS01, respectively. This work is a contribution to the ASSEMBLAGE project funded by the European Commission (EVK3-CT-2002-00090), and was funded by the BLAME project sponsored by the French National Research Agency (ANR-18-CE01-0007) and by the Region Normandie, which supports the scientific consortium SCALE UMR CNRS 3730. L.G. was supported by internal grants from Woods Hole Oceanographic Institution. Data presented in this study are available in the supplementary material.

## Appendix A. Supplementary data

Supplementary data to this article can be found online at <https://doi.org/10.1016/j.quascirev.2019.106136>.

## References

- Árkai, P., 1991. Chlorite crystallinity: an empirical approach and correlation with illite crystallinity, coal rank and mineral facies as exemplified by Palaeozoic and Mesozoic rocks of northeast Hungary. *J. Metamorph. Geol.* 9, 723–734. <https://doi.org/10.1111/j.1525-1314.1991.tb00561.x>.
- Árkai, P., Faryad, S.W., Vidal, O., Balogh, K., 2003. Very low-grade metamorphism of sedimentary rocks of the Meliata unit, Western Carpathians, Slovakia: implications of phyllosilicate characteristics. *Int. J. Earth Sci.* 92, 68–85. <https://doi.org/10.1007/s00531-002-0303-x>.
- Asch, K., Bellenberg, S., Commission for geological Map of the World, 2005. The 1: 5 million international geological map of Europe and adjacent areas (IGME 5000). Bundesanstalt für Geowissenschaften und Rohstoffe.
- Badertscher, S., Fleitmann, D., Cheng, H., Edwards, R.L., Gökür, O.M., Zumbühl, A., Leuenberger, M., Tüysüz, O., 2011. Pleistocene water intrusions from the Mediterranean and Caspian seas into the Black Sea. *Nat. Geosci.* 4 (4), 236–239. <https://doi.org/10.1038/NGEO1006>.
- Bahr, A., Arz, H.W., Lamy, F., Wefer, G., 2006. Late glacial to Holocene paleoenvironmental evolution of the Black Sea, reconstructed with stable oxygen isotope records obtained on ostracod shells. *Earth Planet. Sci. Lett.* 241 (3–4), 863–875. <https://doi.org/10.1016/j.epsl.2005.10.036>.
- Bahr, A., Lamy, F., Arz, H., Kuhlmann, H., Wefer, G., 2005. Late glacial to Holocene climate and sedimentation history in the NW Black Sea. *Mar. Geol.* 214 (4), 309–322. <https://doi.org/10.1016/j.margeo.2004.11.013>.
- Bahr, A., Lamy, F., Arz, H.W., Major, C., Kwiecien, O., Wefer, G., 2008. Abrupt changes of temperature and water chemistry in the late Pleistocene and early Holocene Black Sea. *Geochem. Geophys. Geosyst.* 9. <https://doi.org/10.1029/2007GC001683>.
- Bard, E., Rostek, F., Turon, J.-L., Gendreau, S., 2000. Hydrological impact of Heinrich events in the subtropical northeast Atlantic. *Science* 289, 1321–1324. <https://doi.org/10.1126/science.289.5483.1321>.
- Bard, E., Rostek, F., Ménot-Combes, G., 2004. Radiocarbon calibration beyond 20,000 <sup>14</sup>C yr BP by means of planktonic foraminifera of the Iberian Margin. *Quat. Res.* 61 (2), 204–214. <https://doi.org/10.1016/j.yqres.2003.11.006>.
- Bard, E., Ménot, G., Rostek, F., Licari, L., Böning, P., Edwards, R.L., Cheng, H., Wang, Y., Heaton, T.J., 2013. Radiocarbon calibration/comparison records based on marine sediments from the Pakistan and Iberian margins. *Radiocarbon* 55 (4), 1999–2019. [https://doi.org/10.2458/azu\\_js\\_rc.55.17114](https://doi.org/10.2458/azu_js_rc.55.17114).
- Barker, S., Diz, P., Vautravers, M.J., Pike, J., Knorr, G., Hall, I.R., Broecker, W.S., 2009. Interhemispheric Atlantic seesaw response during the last deglaciation. *Nature* 457 (7233), 1097. <https://doi.org/10.1038/nature07770>.
- Barker, S., Knorr, G., Edwards, R.L., Parrenin, F., Putnam, A.E., Skinner, L.C., Wolff, E., Ziegler, M., 2011. 800,000 years of abrupt climate variability. *Science* 334 (6054), 347–351. <https://doi.org/10.1126/science.1203580>.
- Bayon, G., Barrat, J.A., Etoubleau, J., Benoit, M., Bollinger, C., Révillon, S., 2009. Determination of rare earth elements, Sc, Y, Zr, Ba, Hf and Th in geological samples by ICP-MS after Tm addition and alkaline fusion. *Geostand. Geoanal. Res.* 33, 51–62. <https://doi.org/10.1111/j.1751-908X.2008.00880.x>.
- Bayon, G., German, C.R., Boella, R.M., Milton, J.A., Taylor, R.N., Nesbitt, R.W., 2002. An improved method for extracting marine sediment fractions and its application to Sr and Nd isotopic analysis. *Chem. Geol.* 187, 179–199. [https://doi.org/10.1016/S0009-2541\(01\)00416-8](https://doi.org/10.1016/S0009-2541(01)00416-8).
- Bayon, G., Toucanne, S., Skonieczny, C., André, L., Bermell, S., Cheron, S., Dennielou, B., Etoubleau, J., Freslon, N., Gauchery, T., Germain, Y., Jorj, S.J., Ménot, G., Monin, L., Ponzevera, E., Rouget, M.-L., Tachikawa, K., Barrat, J.A., 2015. Rare earth elements and neodymium isotopes in world river sediments revisited. *Geochem. Cosmochim. Acta* 170, 17–38. <https://doi.org/10.1016/j.gca.2015.08.001>.
- Becker, P., Seguinot, J., Juvet, G., Funk, M., 2016. Last Glacial Maximum precipitation pattern in the Alps inferred from glacier modelling. *Geogr. Helv.* 71, 173–187. <https://doi.org/10.5194/gf-71-173-2016>.
- Beghin, P., Charbit, S., Dumas, C., Kageyama, M., Ritz, C., 2015. How might the North American ice sheet influence the northwestern Eurasian climate? *Clim. Past Discuss.* 11, 1467–1490. <https://doi.org/10.5194/cp-11-1467-2015>.
- Blöschl, G., Nester, T., Komma, J., Parajka, J., Perdigão, R.A., 2013. The June 2013 flood in the upper Danube basin, and comparisons with the 2002, 1954 and 1899 floods. *Hydrol. Earth Syst. Sci.* 17, 5197–5212. <https://doi.org/10.5194/hess-17-5197-2013>.
- Blum, M.D., Törnqvist, T.E., 2000. Fluvial responses to climate and sea-level change: a review and look forward. *Sedimentology* 47, 2–48. <https://doi.org/10.1046/j.1365-3091.2000.00008.x>.
- Bobos, I., 2012. Characterization of smectite to NH<sub>4</sub>-illite conversion series in the fossil hydrothermal system of Harghita Băi, East Carpathians, Romania. *Am. Mineral.* 97, 962–982. <https://doi.org/10.2138/am.2012.3801>.
- Bonneau, L., Jorj, S.J., Toucanne, S., Silva Jacinto, R., Emmanuel, L., 2014. Millennial-scale response of a western Mediterranean river to late Quaternary climate changes: a view from the deep sea. *J. Geol.* 122, 687–703. <https://doi.org/10.1086/677844>.
- Bonneau, L., Toucanne, S., Bayon, G., Jorj, S.J., Emmanuel, L., Jacinto, R.S., 2017. Glacial erosion dynamics in a small mountainous watershed (Southern French Alps): a source-to-sink approach. *Earth Planet. Sci. Lett.* 458, 366–379. <https://doi.org/10.1016/j.epsl.2016.11.004>.
- Boswell, S.M., Toucanne, S., Creyts, T.T., Hemming, S.R., 2018. Continental-scale transport of sediments by the Baltic Ice Stream elucidated by coupled grain size and Nd provenance analyses. *Earth Planet. Sci. Lett.* 490, 143–150. <https://doi.org/10.1016/j.epsl.2018.03.017>.
- Boswell, S.M., Toucanne, S., Pitel-Roudaut, M., Creyts, T.T., Eynaud, F., Bayon, G., 2019. Enhanced surface melting of the fennoscandian ice sheet during periods of North Atlantic cooling. *Geology* 47 (7), 664–668. <https://doi.org/10.1130/G46370.1>.
- Bousquet, R., Oberhänsli, R., Goffé, B., Wiederkehr, M., Koller, F., Schmid, S.M., Schuster, R., Engi, M., Berger, A., Martinotti, G., 2008. Metamorphism of meta-sediments at the scale of an orogen: a key to the Tertiary geodynamic evolution of the Alps. *Geol. Soc. Lond. Spec. Publ.* 298, 393–411. <https://doi.org/10.1144/SP298.18>.
- Bromley, G., Putnam, A., Borns, H., Lowell, T., Sandford, T., Barrell, D., 2018. Interstadial rise and younger Dryas demise of Scotland's last ice fields. *Paleoceanography and Paleoclimatology* 33, 412–429. <https://doi.org/10.1002/2018PA003341>.
- Bronk Ramsey, C., 2001. Development of the radiocarbon calibration program. *Radiocarbon* 43, 355–363. <https://doi.org/10.1017/S0033822200038212>.
- Bronk Ramsey, C., 2008. Deposition models for chronological records. *Quat. Sci. Rev.* 27 (1–2), 42–60. <https://doi.org/10.1016/j.quascirev.2007.01.019>.
- Bronk Ramsey, C., 2009. Bayesian analysis of radiocarbon dates. *Radiocarbon* 51 (1), 337–360. <https://doi.org/10.1017/S0033822200033865>.
- Bronk Ramsey, C., 2017. Methods for summarizing radiocarbon datasets. *Radiocarbon* 59 (6), 1809–1833. <https://doi.org/10.1017/RDC.2017.108>.
- Bronk Ramsey, C., Lee, S., 2013. Recent and planned developments of the program OxCal. *Radiocarbon* 55, 720–730. <https://doi.org/10.1017/S0033822200057878>.
- Brown, P.A., Kennett, J.P., 1998. Megaflood erosion and meltwater plumbing changes during last North American deglaciation recorded in Gulf of Mexico sediments. *Geology* 26, 599–602. [https://doi.org/10.1130/0091-7613\(1998\)026<0599:MEAMPC>2.3.CO;2](https://doi.org/10.1130/0091-7613(1998)026<0599:MEAMPC>2.3.CO;2).
- Buizert, C., Klinkin, V., Severinghaus, J.P., He, F., Lecavalier, B.S., Kindler, P., White, J.W., 2014. Greenland temperature response to climate forcing during the last deglaciation. *Science* 345 (6201), 1177–1180. <https://doi.org/10.1126/science.1254961>.
- Busschers, F.S., Kasse, C., Van Balen, R.T., Vandenbergh, J., Cohen, K.M., Weerts, H.J.T., Wallinga, J., Johns, C., Cleveringa, P., Bunnik, F.P.M., 2007. Late Pleistocene evolution of the Rhine-Meuse system in the southern North Sea basin: imprints of climate change, sea-level oscillation and glacio-isostasy. *Quat. Sci. Rev.* 26, 3216–3248. <https://doi.org/10.1016/j.quascirev.2007.07.013>.
- Carlson, A.E., Clark, P.U., 2012. Ice sheet sources of sea level rise and freshwater discharge during the last deglaciation. *Rev. Geophys.* 50. <https://doi.org/10.1029/2011RG000371>.
- Chaline, J., Jerz, H., 1984. Arbeitsergebnisse der Subkommission für Europäische Quartärstratigraphie. *Stratotypen des Würm-Glazials. Eiszeitalt. Ggw.* 35, 185–206.
- Chamley, H., 1989. *Clay Sedimentology*. Springer-Verlag, New York.
- Ciulavu, M., Mählmann, R.F., Schmid, S.M., Hofmann, H., Seghedi, A., Frey, M., 2008. Metamorphic evolution of a very low-to low-grade metamorphic core complex (Danubian window) in the South Carpathians. *Geol. Soc. Lond. Spec. Publ.* 298, 281–315. <https://doi.org/10.1144/SP298.14>.
- Clark, P.U., Dyke, A.S., Shakun, J.D., Carlson, A.E., Clark, J., Wohlfarth, B., Mitrovica, J.X., Hostetler, S.W., McCabe, A.M., 2009. The last glacial maximum. *Science* 325, 710–714. <https://doi.org/10.1126/science.1172873>.
- Comiti, F., Mao, L., Penna, D., Dell'Agnese, A., Engel, M., Rathburn, S., Cavalli, M., 2019. Glacier melt runoff controls bedload transport in Alpine catchments. *Earth Planet. Sci. Lett.* 520, 77–86. <https://doi.org/10.1016/j.epsl.2019.05.031>.
- Constantinescu, A.M., Toucanne, S., Dennielou, B., Jorj, S.J., Mulder, T., Lericolais, G., 2015. Evolution of the Danube deep-sea fan since the last glacial maximum: new insights into Black Sea water-level fluctuations. *Mar. Geol.* 367, 50–68. <https://doi.org/10.1016/j.margeo.2015.05.007>.

- Coulthard, T.J., Lewin, J., Macklin, M.G., 2005. Modelling differential catchment response to environmental change. *Geomorphology* 69, 222–241. <https://doi.org/10.1016/j.geomorph.2005.01.008>.
- Covault, J.A., Romans, B.W., Graham, S.A., Fildani, A., Hilley, G.E., 2011. Terrestrial source to deep-sea sink sediment budgets at high and low sea levels: insights from tectonically active Southern California. *Geology* 39, 619–622. <https://doi.org/10.1130/G31801.1>.
- de Leeuw, A., Morton, A., van Baak, C.G.C., Vincent, S.J., 2018. Timing of arrival of the Danube to the Black Sea: provenance of sediments from DSDP site 380/380a. *Terra. Nova* 30, 114–124. <https://doi.org/10.1111/ter.12314>.
- Dean, W.E., Arthur, M.A., 2011. Geochemical Characteristics of Holocene Laminated Sapropel (Unit II) and Underlying Lacustrine Unit III in the Black Sea (Report N° 2010–1323), Open-File Report. <https://doi.org/10.3133/ofr20101323>.
- Debret, M., Copard, Y., Van Exem, A., Bessereau, G., Haeseler, F., Rouzaud, J.N., 2018. The color of refractory organic carbon. *Bull. Soc. Geol. Fr.* 189 (2), 9. <https://doi.org/10.1051/bsgf/2018008>.
- Degens, E.T., Stoffers, P., Golubic, S., 1978. Varve chronology: estimated rates of sedimentation in the Black Sea basin. In: Ross, D.A. (Ed.), *Initial Report of the Deep Sea Drilling Project*, vol. 42. U.S. Government Printing Office, Washington, D.C., pp. 499–508. Part 2.
- Denton, G.H., Alley, R.B., Comer, G.C., Broecker, W.S., 2005. The role of seasonality in abrupt climate change. *Quat. Sci. Rev.* 24 (10–11), 1159–1182. <https://doi.org/10.1016/j.quascirev.2004.12.002>.
- Denton, G.H., Anderson, R.F., Toggweiler, J.R., Edwards, R.L., Schaefer, J.M., Putnam, A.E., 2010. The last glacial termination. *Science* 328 (5986), 1652–1656. <https://doi.org/10.1126/science.1184119>.
- Deuser, W.G., 1972. Late Pleistocene and Holocene history of the Black Sea as indicated by stable isotope studies. *J. Geophys. Res.* 77, 1071–1077.
- Dypvik, H., Harris, N.B., 2001. Geochemical facies analysis of fine-grained siliciclastics using Th/U, Zr/Rb and (Zr+Rb)/Sr ratios. *Chem. Geol.* 181, 131–146. [https://doi.org/10.1016/S0009-2541\(01\)00278-9](https://doi.org/10.1016/S0009-2541(01)00278-9).
- Ehlers, J., Gibbard, P.L., 2004. *Quaternary Glaciations-Extent and Chronology: Part I: Europe*. Elsevier.
- Ellwanger, D., Wielandt-Schuster, U., Franz, M., Simon, T., 2011. The quaternary of the southwest German alpine foreland (Bodensee-Oberschwaben, baden-württemberg, southwest Germany). *Quat. Sci. J.* 60, 306–328. <https://doi.org/10.13285/eg.60.2-3.07>.
- Fitzsimmons, K.E., Marković, S.B., Hambach, U., 2012. Pleistocene environmental dynamics recorded in the loess of the middle and lower Danube basin. *Quat. Sci. Rev.* 41, 104–118. <https://doi.org/10.1016/j.quascirev.2012.03.002>.
- Florineth, D., Schlüchter, C., 2000. Alpine evidence for atmospheric circulation patterns in Europe during the last glacial maximum. *Quat. Res.* 54, 295–308. <https://doi.org/10.1006/qres.2000.2169>.
- Freymond, C.V., Peterse, F., Fischer, L.V., Filip, F., Giosan, L., Eglinton, T.I., 2017. Branched GDGT signals in fluvial sediments of the Danube River basin: method comparison and longitudinal evolution. *Org. Geochem.* 103, 88–96. <https://doi.org/10.1016/j.orggeochem.2016.11.002>.
- Frost, C.D., O'Nions, R.K., Goldstein, S.L., 1986. Mass balance for Nd in the Mediterranean sea. *Chem. Geol.* 55, 45–50. [https://doi.org/10.1016/0009-2541\(86\)90126-9](https://doi.org/10.1016/0009-2541(86)90126-9).
- Gábris, G., Nádor, A., 2007. Long-term fluvial archives in Hungary: response of the Danube and Tisza rivers to tectonic movements and climatic changes during the Quaternary: a review and new synthesis. *Quat. Sci. Rev.* 26, 2758–2782. <https://doi.org/10.1016/j.quascirev.2007.06.030>.
- Garnier, J., Billen, G., Hannon, E., Fonbonne, S., Videnina, Y., Soulie, M., 2002. Modelling the transfer and retention of nutrients in the drainage network of the Danube river. *Estuarine. Coast. Shelf Sci.* 54, 285–308. <https://doi.org/10.1006/ecss.2000.0648>.
- Gibbard, P.L., 1988. The history of the great northwest European rivers during the past three million years. *Philos. Trans. R. Soc. Lond. B Biol. Sci.* 318, 559–602. <https://doi.org/10.1098/rstb.1988.0024>.
- Giosan, L., Donnelly, J.P., Constantinescu, S., Filip, F., Ovejanu, I., Vespremeanu-Stroe, A., Vespremeanu, E., Duller, G.A., 2006. Young Danube delta documents stable Black Sea level since the middle Holocene: morphodynamic, paleogeographic, and archaeological implications. *Geology* 34, 757–760. <https://doi.org/10.1130/G22587.1>.
- Giosan, L., Donnelly, J.P., Vespremeanu, E., Bhattacharya, J.P., Olariu, C., Buonaiuto, F.S., 2005. River delta morphodynamics: examples from the Danube delta. In: Giosan, L., Bhattacharya, J.P. (Eds.), *River Deltas - Concepts, Models and Examples*, vol. 83. SEPM Special Publication, pp. 393–411 (2005).
- Glur, L., Wirth, S.B., Büntgen, U., Gilli, A., Haug, G.H., Schär, C., Beer, J., Anselmetti, F.S., 2013. Frequent floods in the European Alps coincide with cooler periods of the past 2500 years. *Sci. Rep.* 3, 2770. <https://doi.org/10.1038/srep02770>.
- Goldstein, S.J., Jacobsen, S.B., 1988. Nd and Sr isotopic systematics of river water suspended material: implications for crustal evolution. *Earth Planet. Sci. Lett.* 87, 249–265. [https://doi.org/10.1016/0012-821X\(88\)90013-1](https://doi.org/10.1016/0012-821X(88)90013-1).
- Goodbred Jr., S.L., Kuehl, S.A., 2000. Enormous Ganges-Brahmaputra sediment discharge during strengthened early Holocene monsoon. *Geology* 28, 1083–1086. [https://doi.org/10.1130/0091-7613\(2000\)28<1083:EGSDS>2.0.CO;2](https://doi.org/10.1130/0091-7613(2000)28<1083:EGSDS>2.0.CO;2).
- Gorlach, A., Hang, T., Kalm, V., 2017. GIS-based reconstruction of Late Weichselian proglacial lakes in northwestern Russia and Belarus. *Boreas* 46, 486–502. <https://doi.org/10.1111/bor.12223>.
- Grosswald, M.G., 1980. Late Weichselian ice sheet of northern Eurasia. *Quat. Res.* 13, 1–32. [https://doi.org/10.1016/0033-5894\(80\)90080-0](https://doi.org/10.1016/0033-5894(80)90080-0).
- Guichard, F., Carey, S., Arthur, M.A., Sigurdsson, H., Arnold, M., 1993. Tephra from the minoan eruption of santorini in sediments of the Black Sea. *Nature* 363, 610. <https://doi.org/10.1038/363610a0>.
- Habbe, K.A., Rögner, K., 1989. *The Pleistocene Iller Glaciers and their outwash fields*. *Catena Suppl.* 15, 311–328.
- Hallet, B., Hunter, L., Bogen, J., 1996. Rates of erosion and sediment evacuation by glaciers: a review of field data and their implications. *Glob. Planet. Chang.* 12, 213–235. [https://doi.org/10.1016/0921-8181\(95\)00021-6](https://doi.org/10.1016/0921-8181(95)00021-6).
- Heaton, T.J., Bard, E., Hughen, K.A., 2013. Elastic tie-pointing-transferring chronologies between records via a Gaussian process. *Radiocarbon* 55 (4), 1975–1997. [https://doi.org/10.2458/azu\\_js\\_rc.55.17777](https://doi.org/10.2458/azu_js_rc.55.17777).
- Heiri, O., Koinig, K.A., Spötl, C., Barrett, S., Brauer, A., Drescher-Schneider, R., Gaar, D., Ivy-Ochs, S., Kerschner, H., Luetscher, M., 2014. Palaeoclimate records 60–8 ka in the Austrian and Swiss Alps and their forelands. *Quat. Sci. Rev.* 106, 186–205. <https://doi.org/10.1016/j.quascirev.2014.05.021>.
- Henry, F., Jeandel, C., Dupre, B., Minster, J.-F., 1994. Particulate and dissolved Nd in the western Mediterranean Sea: sources, fate and budget. *Mar. Chem.* 45, 283–305. [https://doi.org/10.1016/0304-4203\(94\)90075-2](https://doi.org/10.1016/0304-4203(94)90075-2).
- Hinderer, M., 2001. Late Quaternary denudation of the Alps, valley and lake fillings and modern river loads. *Geodin. Acta* 14, 231–263. <https://doi.org/10.1080/0985311.2001.11432446>.
- Hinderer, M., Kastowski, M., Kamelger, A., Bartolini, C., Schlunegger, F., 2013. River loads and modern denudation of the Alps: a review. *Earth Sci. Rev.* 118, 11–44. <https://doi.org/10.1016/j.earscirev.2013.01.001>.
- Hughes, A.L.C., Gyllencreutz, R., Lohne, Ø.S., Mangerud, J., Svendsen, J.I., 2016. The last Eurasian ice sheets - a chronological database and time-slice reconstruction, DATED-1. *Boreas* 45, 1–45. <https://doi.org/10.1111/bor.12142>.
- Huybers, P., 2006. Early Pleistocene glacial cycles and the integrated summer insolation forcing. *Science* 313, 508–511. <https://doi.org/10.1126/science.1125249>.
- Ivy-Ochs, S., 2015. Glacier variations in the European Alps at the end of the last glaciation. *Cuadernos de Investigación Geográfica* 41, 295. <https://doi.org/10.18172/cig.2750>.
- Ivy-Ochs, S., Kerschner, H., Reuther, A., Preusser, F., Heine, K., Maisch, M., Kubik, P.W., Schlüchter, C., 2008. Chronology of the last glacial cycle in the European Alps. *J. Quat. Sci.* 23, 559–573. <https://doi.org/10.1002/jqs.1202>.
- Ivy-Ochs, S., Lucchesi, S., Baggio, P., Fioraso, G., Gianotti, F., Monegato, G., Graf, A.A., Akçar, N., Christl, M., Carraro, F., Forno, M.G., Schlüchter, C., 2018. New geomorphological and chronological constraints for glacial deposits in the Rivoli-Avigliana end-moraine system and the lower Susa Valley (Western Alps, NW Italy). *J. Quat. Sci.* 33, 550–562. <https://doi.org/10.1002/jqs.3034>.
- Ivy-Ochs, S., Schäfer, J., Kubik, P.W., Synal, H.-A., Schlüchter, C., 2004. Timing of deglaciation on the northern Alpine foreland (Switzerland). *Eclogae Geol. Helv.* 97, 47–55.
- Jacobsen, S.B., Wasserburg, G.J., 1980. Sm-Nd isotopic evolution of chondrites. *Earth Planet. Sci. Lett.* 50, 139–155. [https://doi.org/10.1016/0012-821X\(80\)90125-9](https://doi.org/10.1016/0012-821X(80)90125-9).
- Jacq, K., Perrette, Y., Fanget, B., Sabatier, P., Coquin, D., Martínez-Lamas, R., Debret, M., Arnaud, F., 2019. High-resolution prediction of organic matter concentration with hyperspectral imaging on a sediment core. *Sci. Total Environ.* 663, 236–244. <https://doi.org/10.1016/j.scitotenv.2019.01.320>.
- Jaeger, J.M., Koppes, M.N., 2016. The role of the cryosphere in source-to-sink systems. *Earth Sci. Rev.* 153, 43–76. <https://doi.org/10.1016/j.earscirev.2015.09.011>.
- Jiao, R., Herman, F., Beyssac, O., Adatte, T., Cox, S.C., Nelson, F.E., Neil, H.L., 2018. Erosion of the southern Alps of New Zealand during the last deglaciation. *Geology* 46, 975–978. <https://doi.org/10.1130/G45160.1>.
- Jones, G.A., Gagnon, A.R., 1994. Radiocarbon chronology of Black Sea sediments. *Deep-Sea Res. Part I: Oceanogr.* 41, 531–557. [https://doi.org/10.1016/0967-0637\(94\)90094-9](https://doi.org/10.1016/0967-0637(94)90094-9).
- Juteau, M., Michard, A., Albareda, F., 1986. The Pb-Sr-Nd isotope geochemistry of some recent circum-Mediterranean granites. *Contrib. Mineral. Petrol.* 92, 331–340.
- Karabanov, A.K., Matveyev, A.V., 2011. The Pleistocene Glaciations in Belarus. *Quaternary Sciences*. Elsevier, pp. 29–35. <https://doi.org/10.1016/B978-0-444-53447-7.00003-9>.
- Kasse, B., Bohncke, S.J.P., Vandenbergh, J., Gábris, G., 2010. Fluvial style changes during the last glacial-interglacial transition in the middle Tisza valley (Hungary). *PGA (Proc. Geol. Assoc.)* 121, 180–194. <https://doi.org/10.1016/j.pgeola.2010.02.005>.
- Ker, S., Riboulot, V., 2015. GHASS Cruise, R/V Pourquoi Pas? <https://doi.org/10.17600/15000500>.
- Kisch, H.J., 1991. Illite crystallinity: recommendations on sample preparation, X-ray diffraction settings, and interlaboratory samples. *J. Metamorph. Geol.* 9, 665–670. <https://doi.org/10.1111/j.1525-1314.1991.tb00556.x>.
- Kiss, P., Géméling, K., Molnár, F., Pécskay, Z., 2010. Geochemistry of Sarmatian volcanic rocks in the Tokaj Mts (NE Hungary) and their relationship to hydrothermal mineralization. *Cent. Eur. Geol.* 53, 377–403. <https://doi.org/10.1556/CEuGeol.53.2010.4.3>.
- Kolla, V., Perlmutter, M.A., 1993. Timing of turbidite sedimentation on the Mississippi Fan. *AAPG Bull.* 77, 1129–1141.
- Krumm, H., Petschick, R., Wolf, M., 1988. From diagenesis to anchimetamorphism, upper Austroalpine sedimentary cover in Bavaria and Tyrol. *Geodin. Acta* 2, 33–47. <https://doi.org/10.1080/0985311.1988.1105154>.
- Kubler, B., 1967. La cristallinité de l'illite et les zones tout à fait supérieures du métamorphisme. *Etages tectoniques* 105–121.



- Kwiecien, O., Arz, H.W., Lamy, F., Wulf, S., Bahr, A., Röhl, U., Haug, G.H., 2008. Estimated reservoir ages of the black sea since the last glacial. *Radiocarbon* 50, 99–118. <https://doi.org/10.1017/S0033822200043393>.
- Larsen, N.K., Knudsen, K.L., Krohn, C.F., Kronborg, C., Murray, A.S., Nielsen, O.B., 2009. Late Quaternary ice sheet, lake and sea history of southwest Scandinavia—a synthesis. *Boreas* 38, 732–761. <https://doi.org/10.1111/j.1502-3885.2009.00101.x>.
- Laskar, J., Robutel, P., Joutel, F., Gastineau, M., Correia, A.C.M., Levrard, B., 2004. A long-term numerical solution for the insolation quantities of the Earth. *Astron. Astrophys.* 428, 261–285. <https://doi.org/10.1051/0004-6361:20041335>.
- Lehmann, B., Herman, F., Valla, P.G., King, G.E., Biswas, R.H., Ivy-Ochs, S., Steinemann, O., Christl, M., 2020. Postglacial erosion of bedrock surfaces and deglaciation timing: new insights from the Mont Blanc massif (western Alps). *Geology* 48. <https://doi.org/10.1130/G46585.1>.
- Lericolais, G., 2004. ASSEMBLAGE-1 Cruise, R/V Marion Dufresne. <https://doi.org/10.17600/4200070>.
- Lericolais, G., Bourget, J., Popescu, I., Jermannaud, P., Mulder, T., Jorjy, S., Panin, N., 2013. Late Quaternary deep-sea sedimentation in the western Black Sea: new insights from recent coring and seismic data in the deep basin. *Glob. Planet. Chang.* 103, 232–247. <https://doi.org/10.1016/j.gloplacha.2012.05.002>.
- Lericolais, G., Guichard, F., Morigi, C., Popescu, I., Bulois, C., Gillet, H., Ryan, W.B.F., 2011. Assessment of Black Sea water-level fluctuations since the last glacial maximum. *Geol. Geoarchaeology of the Black Sea Reg.: Beyond the Flood Hypothesis* 473, 33.
- Ludwig, P., Schaffernicht, E.J., Shao, Y., Pinto, J.G., 2016. Regional atmospheric circulation over Europe during the last glacial maximum and its links to precipitation. *J. Geophys. Res.: Atmosphere* 121, 2130–2145. <https://doi.org/10.1002/2015JD024444>.
- Luetscher, M., Boch, R., Sodemann, H., Spötl, C., Cheng, H., Edwards, R.L., Frisia, S., Hof, F., Müller, W., 2015. North Atlantic storm track changes during the last glacial maximum recorded by alpine speleothems. *Nat. Commun.* 6 <https://doi.org/10.1038/ncomms7344>.
- Macklin, M.G., Benito, G., Gregory, K.J., Johnstone, E., Lewin, J., Michczyńska, D.J., Soja, R., Starkel, L., Thorndycraft, V.R., 2006. Past hydrological events reflected in the Holocene fluvial record of Europe. *Catena* 66, 145–154. <https://doi.org/10.1016/j.catena.2005.07.015>.
- Macklin, M.G., Johnstone, E., Lewin, J., 2005. Pervasive and long-term forcing of Holocene river instability and flooding in Great Britain by centennial-scale climate change. *Holocene* 15, 937–943. <https://doi.org/10.1191/0959683605hl867ft>.
- Macklin, M.G., Lewin, J., 2003. River sediments, great floods and centennial-scale Holocene climate change. *J. Quat. Sci.* 18, 101–105. <https://doi.org/10.1002/jqs.751>.
- Macklin, M.G., Lewin, J., Woodward, J.C., 2012. The fluvial record of climate change. *Philos. Trans. R. Soc. A Math. Phys. Eng. Sci.* 370, 2143–2172. <https://doi.org/10.1098/rsta.2011.0608>.
- Magyar, E.K., Pál, I., Vincze, I., Veres, D., Jakab, G., Braun, M., Szalai, Z., Szabo, Z., Korponai, J., 2019. Warm Younger Dryas summers and early late glacial spread of temperate deciduous trees in the Pannonian Basin during the last glacial termination (20–9 kyr cal BP). *Quat. Sci. Rev.* 225, 105980. <https://doi.org/10.1016/j.quascirev.2019.105980>.
- Major, C., Ryan, W., Lericolais, G., Hajdas, I., 2002. Constraints on Black Sea outflow to the Sea of Marmara during the last glacial–interglacial transition. *Mar. Geol.* 190 (1–2), 19–34. [https://doi.org/10.1016/S0025-3227\(02\)00340-7](https://doi.org/10.1016/S0025-3227(02)00340-7).
- Major, C.O., Goldstein, S.L., Ryan, W.B., Lericolais, G., Piotrowski, A.M., Hajdas, I., 2006. The co-evolution of Black Sea level and composition through the last deglaciation and its paleoclimatic significance. *Quat. Sci. Rev.* 25, 2031–2047. <https://doi.org/10.1016/j.quascirev.2006.01.032>.
- Makos, M., Dzierżek, J., Nitychoruk, J., Zreda, M., 2014. Timing of glacier advances and climate in the high tatra mountains (western Carpathians) during the last glacial maximum. *Quat. Res.* 82, 1–13. <https://doi.org/10.1016/j.yqres.2014.04.001>.
- Makos, M., Nitychoruk, J., Zreda, M., 2013. Deglaciation chronology and paleoclimate of the pięciu stawów polskich/roztoki valley, high tatra mountains, western Carpathians, since the last glacial maximum, inferred from 36Cl exposure dating and glacier–climate modelling. *Quat. Int.* 293, 63–78. <https://doi.org/10.1016/j.quaint.2012.01.016>.
- Makos, M., Rinterknecht, V., Braucher, R., Toloczko-Pasek, A., Arnold, M., Aumaître, G., Bourlès, D., Keddadouche, K., 2018. Last glacial maximum and lateglacial in the polish high tatra mountains - revised deglaciation chronology based on the 10 Be exposure age dating. *Quat. Sci. Rev.* 187, 130–156. <https://doi.org/10.1016/j.quascirev.2018.03.006>.
- Makshaev, R.R., Svitoch, A.A., 2016. Chocolate clays of the northern caspian sea region: distribution, structure, and origin. *Quat. Int.* 409, 44–49. <https://doi.org/10.1016/j.quaint.2015.07.018>.
- Mangerud, J., Jakobsson, M., Alexanderson, H., Astakhov, V., Clarke, G.K., Henriksen, M., Hjort, C., Krinner, G., Lunkka, J.-P., Möller, P., 2004. Ice-dammed lakes and rerouting of the drainage of northern Eurasia during the Last Glaciation. *Quat. Sci. Rev.* 23, 1313–1332. <https://doi.org/10.1016/j.quascirev.2003.12.009>.
- Marković, S.B., Stevens, T., Kukla, G.J., Hambach, U., Fitzsimmons, K.E., Gibbard, P., Buggle, B., Zech, M., Guo, Z., Hao, Q., Wu, H., O'Hara Dhand, K., Smalley, I.J., Újvári, G., Sümegi, P., Timar-Gabor, A., Veres, D., Sirocko, F., Vasiljević, D.A., Jary, Z., Svensson, A., Jović, V., Lehmkuhl, F., Kovács, J., Svirčev, Z., 2015. Danube loess stratigraphy - towards a pan-European loess stratigraphic model. *Earth Sci. Rev.* 148, 228–258. <https://doi.org/10.1016/j.earscirev.2015.06.005>.
- Marret, F., Mudie, P., Aksu, A., Hiscott, R.N., 2009. A Holocene dinocyst record of a two-step transformation of the Neoeuxinian brackish water lake into the Black Sea. *Quat. Int.* 197 (1–2), 72–86. <https://doi.org/10.1016/j.quaint.2007.01.010>.
- Matenco, L., Andriessen, P., 2013. Quantifying the mass transfer from mountain ranges to deposition in sedimentary basins: source to sink studies in the Danube Basin–Black Sea system. *Glob. Planet. Chang.* 103, 1–18. <https://doi.org/10.1016/j.gloplacha.2013.01.003>.
- Mayr, C., Stojakowits, P., Lempe, B., Blaauw, M., Diersche, V., Grohgan, M., Correa, M.L., Ohlendorf, C., Reimer, P., Zolitschka, B., 2019. High-resolution geochemical record of environmental changes during MIS 3 from the northern Alps (Nesseltalgraben, Germany). *Quat. Sci. Rev.* 218, 122–136. <https://doi.org/10.1016/j.quascirev.2019.06.013>.
- Ménot, G., Bard, E., Rostek, F., Weijers, J.W., Hopmans, E.C., Schouten, S., Damsté, J.S.S., 2006. Early reactivation of European rivers during the last deglaciation. *Science* 313, 1623–1625. <https://doi.org/10.1126/science.1130511>.
- Milliman, J.D., Farnsworth, K.L., 2013. *River Discharge to the Coastal Ocean: a Global Synthesis*. Cambridge University Press.
- Milliman, J.D., Syvitski, J.P., 1992. Geomorphic/tectonic control of sediment discharge to the ocean: the importance of small mountainous rivers. *J. Geol.* 100, 525–544. <https://doi.org/10.1086/629606>.
- Misch, D., Wegener, E., Gross, D., Sachsenhofer, R.F., Rachetti, A., Gratzner, R., 2018. Mineralogy and facies variations of devonian and carboniferous shales in the Ukrainian Dniepr-Donets basin. *Aust. J. Earth Sci.* 111, 15–25. <https://doi.org/10.17738/ajes.2018.0002>.
- Mol, J., Vandenbergh, J., Kasse, C., 2000. River response to variations of periglacial climate in mid-latitude Europe. *Geomorphology* 33, 131–148. [https://doi.org/10.1016/S0169-555X\(99\)00126-9](https://doi.org/10.1016/S0169-555X(99)00126-9).
- Monegato, G., Ravazzi, C., Donegana, M., Pini, R., Calderoni, G., Wick, L., 2007. Evidence of a two-fold glacial advance during the last glacial maximum in the Tagliamento end moraine system (eastern Alps). *Quat. Res.* 68, 284–302. <https://doi.org/10.1016/j.yqres.2007.07.002>.
- Monegato, G., Scardia, G., Hajdas, I., Rizzini, F., Piccin, A., 2017. The Alpine LGM in the boreal ice-sheets game. *Sci. Rep.* 7, 2078. <https://doi.org/10.1038/s41598-017-02148-7>.
- Mulder, T., Alexander, J., 2001. The physical character of subaqueous sedimentary density flows and their deposits. *Sedimentology* 48, 269–299. <https://doi.org/10.1046/j.1365-3091.2001.00360.x>.
- Mulder, T., Syvitski, J.P., 1995. Turbidity currents generated at river mouths during exceptional discharges to the world oceans. *J. Geol.* 103, 285–299. <https://doi.org/10.1086/629747>.
- Mulder, T., Syvitski, J.P., Migeon, S., Faugeres, J.-C., Savoye, B., 2003. Marine hyperpycnal flows: initiation, behavior and related deposits. A review. *Mar. Pet. Geol.* 20, 861–882. <https://doi.org/10.1016/j.marpetgeo.2003.01.003>.
- Mulder, T., Syvitski, J.P., Skene, K.I., 1998. Modeling of erosion and deposition by turbidity currents generated at river mouths. *J. Sediment. Res.* 68, 124–137. <https://doi.org/10.2110/jsr.68.124>.
- Müller, G., Quakernaat, J., 1969. *Diffractionmetric clay mineral analysis of recent sediments of Lake Constance (Central Europe)*. *Contrib. Mineral. Petrol.* 22, 268–275.
- Muttoni, G., Carcano, C., Garzanti, E., Ghielmi, M., Piccin, A., Pini, R., Rogledi, S., Sciunnach, D., 2003. Onset of major pleistocene glaciations in the Alps. *Geology* 31, 989–992. <https://doi.org/10.1130/G19445.1>.
- Nievergelt, P., Liniger, M., Froitzheim, N., Mählmann, R.F., 1996. Early to mid-Tertiary crustal extension in the Central Alps: the Turba mylonite zone (eastern Switzerland). *Tectonics* 15, 329–340. <https://doi.org/10.1029/93TC02312>.
- Nikishin, A.M., Korotaev, M.V., Ershov, A.V., Brunet, M.-F., 2003. The Black Sea basin: tectonic history and Neogene–Quaternary rapid subsidence modelling. *Sedim. Geol.* 156, 149–168. [https://doi.org/10.1016/S0037-0738\(02\)00286-5](https://doi.org/10.1016/S0037-0738(02)00286-5).
- Normark, W.R., Piper, D.J., 1991. Initiation processes and flow evolution of turbidity currents: implications for the depositional record. *SEPM Spec. Publ.* 46, 207–230.
- Oerlemans, J., Greuell, W., Denby, B., van de Wal, R., 2001. 10 years of mass-balance measurements along a transect near Kangerlussuaq, central West Greenland. *J. Glaciol.* 47, 157–158. <https://doi.org/10.3189/172756501781832458>.
- Panin, N., Jipa, D., 2002. Danube River sediment input and its interaction with the north-western Black Sea. *Estuar. Coast Shelf Sci.* 54, 551–562. <https://doi.org/10.1006/ecs.2000.0664>.
- Panin, N., Panin, S., Herz, N., Noakes, J.E., 1983. Radiocarbon dating of Danube delta deposits. *Quat. Res.* 19, 249–255. [https://doi.org/10.1016/0033-5894\(83\)90008-X](https://doi.org/10.1016/0033-5894(83)90008-X).
- Parajka, J., Kohnová, S., Bálint, G., Barbuc, M., Borga, M., Claps, P., Cheval, S., Dumitrescu, A., Gaume, E., Hlavčová, K., 2010. Seasonal characteristics of flood regimes across the Alpine–Carpathian range. *J. Hydrol.* 394, 78–89. <https://doi.org/10.1016/j.jhydrol.2010.05.015>.
- Pastre, J.-F., Limondin-Lozouet, N., Leroyer, C., Ponel, P., Fontugne, M., 2003. River system evolution and environmental changes during the Lateglacial in the Paris Basin (France). *Quat. Sci. Rev.* 22, 2177–2188. [https://doi.org/10.1016/S0277-3791\(03\)00147-1](https://doi.org/10.1016/S0277-3791(03)00147-1).
- Pellegrini, C., Asioli, A., Bohacs, K.M., Drexler, T.M., Feldman, H.R., Sweet, M.L., Maselli, V., Rovere, M., Gamberi, F., Dalla Valle, G., 2018. The late Pleistocene Po River lowstand wedge in the Adriatic Sea: controls on architecture variability and sediment partitioning. *Mar. Pet. Geol.* 96, 16–50. <https://doi.org/10.1016/j.marpetgeo.2018.03.002>.
- Pellegrini, C., Maselli, V., Gamberi, F., Asioli, A., Bohacs, K.M., Drexler, T.M.,

- Trincardi, F., 2017. How to make a 350-m-thick lowstand systems tract in 17,000 years: the Late Pleistocene Po River (Italy) lowstand wedge. *Geology* 45, 327–330. <https://doi.org/10.1130/G38848.1>.
- Piper, D.J., Normark, W.R., 2009. Processes that initiate turbidity currents and their influence on turbidites: a marine geology perspective. *J. Sediment. Res.* 79, 347–362. <https://doi.org/10.2110/jsr.2009.046>.
- Popescu, I., Lericolais, G., Panin, N., Normand, A., Dinu, C., Le Drezen, E., 2004. The Danube submarine canyon (Black Sea): morphology and sedimentary processes. *Mar. Geol.* 206 (1–4), 249–265. <https://doi.org/10.1016/j.margeo.2004.03.003>.
- Popescu, I., Lericolais, G., Panin, N., Wong, H.K., Droz, L., 2001. Late quaternary channel avulsions on the Danube deep-sea fan, Black Sea. *Mar. Geol.* 179, 25–37. [https://doi.org/10.1016/S0025-3227\(01\)00197-9](https://doi.org/10.1016/S0025-3227(01)00197-9).
- Preusser, F., 2004. Towards a chronology of the late pleistocene in the northern alpine foreland. *Boreas* 33, 195–210. <https://doi.org/10.1111/j.1502-3885.2004.tb01141.x>.
- Preusser, F., Graf, H.R., Keller, O., Krayss, E., Schlüchter, C., 2011. Quaternary glacial history of northern Switzerland. *Quat. Sci. J.* 60, 282–305. <https://doi.org/10.3285/eg.60.2-3.06>.
- Rainer, T., Herlec, U., Rantitsch, G., Sachsenhofer, R.F., Vrabec, M., 2002. Organic matter maturation vs clay mineralogy: a comparison for Carboniferous to Eocene sediments from the Alpine-Dinaride junction (Slovenia, Austria). *Geologija* 45, 513–518.
- Rantitsch, G., 1997. Thermal history of the carnic Alps (southern Alps, Austria) and its palaeogeographic implications. *Tectonophysics* 272, 213–232. [https://doi.org/10.1016/S0040-1951\(96\)00259-4](https://doi.org/10.1016/S0040-1951(96)00259-4).
- Rasmussen, S.O., Bigler, M., Blockley, S.P., Blunier, T., Buchardt, S.L., Clausen, H., Cuvjancovic, I., Dahl-Jensen, D., Johnsen, S.J., Fisher, H., Gkinis, V., Guillevic, M., Hoek, W.Z., Lowe, J.J., Pedro, J.B., Poop, T., Walker, I.K., Wheatley, J.J., Winstrup, M., 2014. A stratigraphic framework for abrupt climatic changes during the Last Glacial period based on three synchronized Greenland ice-core records: refining and extending the INTIMATE event stratigraphy. *Quat. Sci. Rev.* 106, 14–28. <https://doi.org/10.1016/j.quascirev.2014.09.007>.
- Ravazzi, C., Pini, R., Badino, F., De Amicis, M., Londeix, L., Reimer, P.J., 2014. The latest LGM culmination of the Garda Glacier (Italian Alps) and the onset of glacial termination. Age of glacial collapse and vegetation chronosequence. *Quat. Sci. Rev.* 105, 26–47. <https://doi.org/10.1016/j.quascirev.2014.09.014>.
- Reber, R., Akcar, N., Ivy-Ochs, S., Tikhomirov, D., Burkhalter, R., Zahno, C., Lüthold, A., Kubik, P., Vockenhuber, C., Schlüchter, C., 2014. Deglaciation of the reuss glacier in the Alps at the end of the last glacial maximum. *Swiss J. Geosci.* 107, 293–307. <https://doi.org/10.1007/s00015-014-0169-5>.
- Reitner, J.M., 2012. Challenges in deciphering the last glacial cycle in eastern Alps: examples from the drau glacier system. *Quat. Int.* 279, 398. <https://doi.org/10.1016/j.quaint.2012.08.1255>.
- Reitner, J.M., 2007. Glacial dynamics at the beginning of Termination I in the Eastern Alps and their stratigraphic implications. *Quat. Int.* 164, 64–84. <https://doi.org/10.1016/j.quaint.2006.12.016>.
- Reuther, A.U., Urdea, P., Geiger, C., Ivy-Ochs, S., Niller, H.-P., Kubik, P.W., Heine, K., 2007. Late pleistocene glacial chronology of the pietrele valley, rezeat mountains, southern Carpathians constrained by  $^{10}\text{Be}$  exposure ages and pedological investigations. *Quat. Int.* 164, 151–169. <https://doi.org/10.1016/j.quaint.2006.10.011>.
- Revel, M., Ducassou, E., Grousset, F.E., Bernasconi, S.M., Migeon, S., Révillon, S., Mascle, J., Murat, A., Zaragosi, S., Bosch, D., 2010. 100,000 years of African monsoon variability recorded in sediments of the Nile margin. *Quat. Sci. Rev.* 29, 1342–1362. <https://doi.org/10.1016/j.quascirev.2010.02.006>.
- Riboulot, V., Cattaneo, A., Scalabrini, C., Gailliot, A., Jouet, G., Ballas, G., Marsset, T., Garziglia, S., Ker, S., 2017. Control of the geomorphology and gas hydrate extent on widespread gas emissions offshore Romania. *Bull. Soc. Geol. Fr.* 188 (4), 26. <https://doi.org/10.1051/bsgf/2017182>.
- Ross, D.A., Degens, E.T., MacIvaine, J., 1970. Black Sea: recent sedimentary history. *Science* 170, 163–165. <https://doi.org/10.1126/science.170.3954.163>.
- Ross, D.A., Degens, E.T., 1974. Recent sediments of Black Sea. In: Degens, E.T., Ross, D.A. (Eds.), *The Black Sea: Geology, Chemistry, and Biology*. American Association of Petroleum Geologists, Tulsa, pp. 183–199.
- Rossato, S., Mozzi, P., 2016. Inferring LGM sedimentary and climatic changes in the southern Eastern Alps foreland through the analysis of a  $^{14}\text{C}$  ages database (Brenta megafan, Italy). *Quat. Sci. Rev.* 148, 115–127. <https://doi.org/10.1016/j.quascirev.2016.07.013>.
- Ryan, W.B., Pitman III, W.C., Major, C.O., Shimkus, K., Moskalenko, V., Jones, G.A., Dimitrov, P., Gorür, N., Saking, M., Yüce, H., 1997. An abrupt drowning of the Black Sea shelf. *Mar. Geol.* 138, 119–126. [https://doi.org/10.1016/S0025-3227\(97\)00007-8](https://doi.org/10.1016/S0025-3227(97)00007-8).
- Sanchez Goni, M.F., Harrison, S.P., 2010. Millennial-scale climate variability and vegetation changes during the Last Glacial: concepts and terminology. *Quat. Sci. Rev.* 29, 2823–2827. <https://doi.org/10.1016/j.quascirev.2009.11.014>.
- Schenk, F., Välranta, M., Muschitiello, F., Tarasov, L., Heikkilä, M., Björck, S., Brandefelt, J., Johansson, A.V., Näslund, J.-O., Wohlfarth, B., 2018. Warm summers during the Younger Dryas cold reversal. *Nat. Commun.* 9. <https://doi.org/10.1038/s41467-018-04071-5>.
- Sanchi, L., Ménot, G., Bard, E., 2014. Insights into continental temperatures in the northwestern Black Sea area during the Last Glacial period using branched tetraether lipids. *Quat. Sci. Rev.* 84, 98–108. <https://doi.org/10.1016/j.quascirev.2013.11.013>.
- Schmieder, K., Schünemann, B., Schröder, H.G., 2004. Spatial patterns of surface sediment variables in the littoral zone of Lake Constance (Germany). *Arch. Hydrobiol.* 161, 455–468. <https://doi.org/10.1127/0003-9136/2004/0161-0455>.
- Schramm, J.-M., 1991. The permian–triassic of the gartnerkofel-1 core (carnic Alps, Austria): illite crystallinity in shaly sediments and its comparison with prevariscan sequences. *Abh Geol BA* 45, 69–77.
- Schumilovskikh, L.S., Fleitmann, D., Nowaczyk, N.R., Behling, H., Marret, F., Wegwerth, A., Arz, H.W., 2014. Orbital and millennial-scale environmental changes between 64 and 25 ka BP recorded in Black Sea sediments. *Clim. Past* 10, 939–945. <https://doi.org/10.5194/cp-10-939-2014>.
- Seguinot, J., Jouvett, G., Huss, M., Funk, M., Ivy-Ochs, S., Preusser, F., 2018. Modelling last glacial cycle ice dynamics in the Alps. *Cryosphere Discuss.* 1–30. <https://doi.org/10.5194/tc-2018-8>.
- Sidorchuk, A.Y., Panin, A.V., Borisova, O.K., 2011. Surface runoff to the Black Sea from the east European plain during last glacial maximum–late glacial time. *Spec. Pap. Geol. Soc. Am.* 473, 1–25.
- Sidorchuk, A.Y., Panin, A.V., Borisova, O.K., 2008. Climate-induced changes in surface runoff on the North-Eurasian plains during the late glacial and Holocene. *Water Resour.* 35, 386–396. <https://doi.org/10.1134/S0097807808040027>.
- Simpson, G., Castelltort, S., 2012. Model shows that rivers transmit high-frequency climate cycles to the sedimentary record. *Geology* 40, 1131–1134. <https://doi.org/10.1130/G33451.1>.
- Sionneau, T., Bout-Roumazilles, V., Biscaye, P.E., Van Vliet-Lanoe, B., Bory, A., 2008. Clay mineral distributions in and around the Mississippi River watershed and Northern Gulf of Mexico: sources and transport patterns. *Quat. Sci. Rev.* 27, 1740–1751. <https://doi.org/10.1016/j.quascirev.2008.07.001>.
- Skinner, L.C., Fallon, S., Waelbroeck, C., Michel, E., Barker, S., 2010. Ventilation of the deep Southern Ocean and deglacial CO<sub>2</sub> rise. *Science* 328 (5982), 1147–1151. <https://doi.org/10.1126/science.1183627>.
- Skinner, L.C., Muschitiello, F., Scrivner, A.E., 2019. Marine reservoir age variability over the last deglaciation: implications for marine carbon cycling and prospects for regional radiocarbon calibrations. *Paleoceanogr. Paleoclimatol.* <https://doi.org/10.1029/2019PA003667>.
- Sommerwerk, N., Hein, T., Schneider-Jajoby, M., Baumgartner, C., Ostojic, M., Paunovic, M., Bloesch, J., Siber, R., Tockner, K., 2009. The Danube river basin. In: Tockner, K., Robinson, C.T., Uehlinger, U. (Eds.), *Rivers of Europe*, vol. 20092009. Elsevier Ltd., London, UK, pp. 59–113. <https://doi.org/10.1016/B978-0-12-369449-2.00003-5>.
- Soulet, G., Delaigue, G., Vallet-Coulomb, C., Böttcher, M.E., Sonzogni, C., Lericolais, G., Bard, E., 2010. Glacial hydrologic conditions in the Black Sea reconstructed using geochemical pore water profiles. *Earth Planet. Sci. Lett.* 296, 57–66. <https://doi.org/10.1016/j.epsl.2010.04.045>.
- Soulet, G., Giosan, L., Flaux, C., Galy, V., 2019. Using stable carbon isotopes to quantify radiocarbon reservoir age offsets in the coastal Black Sea. *Radiocarbon* 61, 309–318. <https://doi.org/10.1017/RDC.2018.61>.
- Soulet, G., Ménot, G., Garreta, V., Rostek, F., Zaragosi, S., Lericolais, G., Bard, E., 2011a. Black Sea “Lake” reservoir age evolution since the Last Glacial-hydrologic and climatic implications. *Earth Planet. Sci. Lett.* 308 (1–2), 245–258. <https://doi.org/10.1016/j.epsl.2011.06.002>.
- Soulet, G., Ménot, G., Lericolais, G., Bard, E., 2011b. A revised calendar age for the last reconnection of the Black Sea to the global ocean. *Quat. Sci. Rev.* 30, 1019–1026. <https://doi.org/10.1016/j.quascirev.2011.03.001>.
- Soulet, G., Ménot, G., Bayon, G., Rostek, F., Ponzevera, E., Toucanne, S., Lericolais, G., Bard, E., 2013. Abrupt drainage cycles of the fennoscandian ice sheet. *Proc. Natl. Acad. Sci. U.S.A.* 110, 6682–6687. <https://doi.org/10.1073/pnas.1214676110>.
- Spötl, C., Reimer, P.J., Starnberger, R., Reimer, R.W., 2013. A new radiocarbon chronology of Baumkirchen, stratotype for the onset of the Upper Würmian in the Alps: a new radiocarbon chronology of baumkirchen. *J. Quat. Sci.* 28, 552–558. <https://doi.org/10.1002/jqs.2645>.
- Starkel, L., Michczynska, D.J., Gebica, P., Kiss, T., Panin, A., Perşoiu, I., 2015. Climatic fluctuations reflected in the evolution of fluvial systems of Central-Eastern Europe (60–8 ka cal BP). *Quat. Int.* 388, 97–118. <https://doi.org/10.1016/j.quaint.2015.04.017>.
- Starnberger, R., Drescher-Schneider, R., Reitner, J.M., Rodnight, H., Reimer, P.J., Spötl, C., 2013. Late Pleistocene climate change and landscape dynamics in the Eastern Alps: the inner-alpine Unterangerberg record (Austria). *Quat. Sci. Rev.* 68, 17–42. <https://doi.org/10.1016/j.quascirev.2013.02.008>.
- Starnberger, R., Rodnight, H., Spötl, C., 2011. Chronology of the last glacial maximum in the Salzach palaeoglacier area (eastern Alps). *J. Quat. Sci.* 26, 502–510. <https://doi.org/10.1002/jqs.1477>.
- Starnberger, R., Terhorst, B., Rähle, W., Peticzka, R., Haas, J.N., 2009. Palaeoecology of quaternary periglacial environments during OIS-2 in the forefields of the Salzach glacier (upper Austria). *Quat. Int.* 198, 51–61. <https://doi.org/10.1016/j.quaint.2008.06.011>.
- Stoffers, P., Müller, G., 1978. Mineralogy and lithofacies of Black Sea sediments, Leg 42B deep sea drilling project. In: *Initial Reports of the Deep Sea Drilling Project*, vol. 42, pp. 373–411.
- Stroeven, A.P., Hättestrand, C., Kleman, J., Heyman, J., Fabel, D., Fredin, O., Goodfellow, B.W., Harbor, J.M., Jansen, J.D., Olsen, L., 2016. Deglaciation of fennoscandia. *Quat. Sci. Rev.* 147, 91–121. <https://doi.org/10.1016/j.quascirev.2015.09.016>.
- Swierczynski, T., Lauterbach, S., Dulski, P., Delgado, J., Merz, B., Brauer, A., 2013. Mid-to late Holocene flood frequency changes in the northeastern Alps as recorded in varved sediments of Lake Mondsee (Upper Austria). *Quat. Sci. Rev.* 80, 78–90. <https://doi.org/10.1016/j.quascirev.2013.08.018>.
- Tanaka, T., Togashi, S., Kamioka, H., Amakawa, H., Kagami, H., Hamamoto, T.,

- Yuhara, M., Orihashi, Y., Yoneda, S., Shimizu, H., 2000. JNdi-1: a neodymium isotopic reference in consistency with LaJolla neodymium. *Chem. Geol.* 168, 279–281. [https://doi.org/10.1016/S0009-2541\(00\)00198-4](https://doi.org/10.1016/S0009-2541(00)00198-4).
- Toucanne, S., Soulet, G., Freslon, N., Jacinto, R.S., Dennielou, B., Zaragosi, S., Eynaud, F., Bourillet, J.-F., Bayon, G., 2015. Millennial-scale fluctuations of the European Ice Sheet at the end of the last glacial, and their potential impact on global climate. *Quat. Sci. Rev.* 123, 113–133. <https://doi.org/10.1016/j.quascirev.2015.06.010>.
- Toucanne, S., Zaragosi, S., Bourillet, J.F., Cremer, M., Eynaud, F., Van Vliet-Lanoë, B., Pénaud, A., Fontanier, C., Turon, J.L., Cortijo, E., 2009. Timing of massive 'Fleuve Manche' discharges over the last 350 kyr: insights into the European ice-sheet oscillations and the European drainage network from MIS 10 to 2. *Quat. Sci. Rev.* 28, 1238–1256. <https://doi.org/10.1016/j.quascirev.2009.01.006>.
- Toucanne, S., Zaragosi, S., Bourillet, J.-F., Marieu, V., Cremer, M., Kageyama, M., Van Vliet-Lanoë, B., Eynaud, F., Turon, J.-L., Gibbard, P.L., 2010. The first estimation of Fleuve Manche palaeoriver discharge during the last deglaciation: evidence for Fennoscandian ice sheet meltwater flow in the English Channel ca 20–18 ka ago. *Earth Planet. Sci. Lett.* 290, 459–473. <https://doi.org/10.1016/j.epsl.2009.12.050>.
- Tudryn, A., Leroy, S.A., Toucanne, S., Gibert-Brunet, E., Tucholka, P., Lavrushin, Y.A., Dufaure, O., Miska, S., Bayon, G., 2016. The Ponto-Caspian basin as a final trap for southeastern Scandinavian Ice-Sheet meltwater. *Quat. Sci. Rev.* 148, 29–43. <https://doi.org/10.1016/j.quascirev.2016.06.019>.
- Újvári, G., Varga, A., Ramos, F.C., Kovács, J., Németh, T., Stevens, T., 2012. Evaluating the use of clay mineralogy, Sr–Nd isotopes and zircon U–Pb ages in tracking dust provenance: an example from loess of the Carpathian Basin. *Chem. Geol.* 304, 83–96. <https://doi.org/10.1016/j.chemgeo.2012.02.007>.
- Van Exem, A., Debret, M., Copard, Y., Verpoorter, C., De Wet, G., Lecoq, N., Sorrel, P., Werner, A., Roof, S., Laignel, B., 2019. New source-to-sink approach in an arctic catchment based on hyperspectral core-logging (Lake Linné, Svalbard). *Quat. Sci. Rev.* 203, 128–140. <https://doi.org/10.1016/j.quascirev.2018.10.038>.
- Van Husen, D., 2004. Quaternary glaciations in Austria. In: *Developments in Quaternary Sciences*. Elsevier, pp. 1–13.
- van Husen, D., 2000. Geological processes during the quaternary. *Mittl. Osterreichischen Geol. Ges.* 92, 135–156.
- Vandenbergh, J., 2003. Climate forcing of fluvial system development: an evolution of ideas. *Quat. Sci. Rev.* 22, 2053–2060. [https://doi.org/10.1016/S0277-3791\(03\)00213-0](https://doi.org/10.1016/S0277-3791(03)00213-0).
- Vandenbergh, J., 2002. The relation between climate and river processes, landforms and deposits during the Quaternary. *Quat. Int.* 91, 17–23. [https://doi.org/10.1016/S1040-6182\(01\)00098-2](https://doi.org/10.1016/S1040-6182(01)00098-2).
- Vidal, L., Menot, G., Joly, C., Bruneton, H., Rostek, F., Çağatay, M.N., Major, C., Bard, E., 2010. Hydrology in the Sea of Marmara during the last 23 ka: implications for timing of Black Sea connections and sapropel deposition. *Paleoceanography* 25. <https://doi.org/10.1029/2009PA001735>.
- Vishnevskaya, V.S., Sedaeva, K.M., 2000. Specific features of early-middle carboniferous sedimentation in the southern part of the east European platform. *Lithol. Miner. Resour.* 35, 455–465.
- Wang, Y.J., Cheng, H., Edwards, R.L., An, Z.S., Wu, J.Y., Shen, C.C., Dorale, J.A., 2001. A high-resolution absolute-dated late Pleistocene monsoon record from Hulu Cave, China. *Science* 294 (5550), 2345–2348. <https://doi.org/10.1126/science.1064618>.
- Wegwerth, A., Kaiser, J., Dellwig, O., Shumilovskikh, L.S., Nowaczyk, N.R., Arz, H.W., 2016. Northern hemisphere climate control on the environmental dynamics in the glacial Black Sea 'Lake'. *Quat. Sci. Rev.* 135, 41–53. <https://doi.org/10.1016/j.quascirev.2016.01.016>.
- Wirsig, C., Zasadni, J., Ivy-Ochs, S., Christl, M., Kober, F., Schlüchter, C., 2016. A deglaciation model of the Oberhasli, Switzerland. *J. Quat. Sci.* 31, 46–59. <https://doi.org/10.1002/jqs.2831>.
- Wirth, S.B., Glur, L., Gilli, A., Anselmetti, F.S., 2013. Holocene flood frequency across the Central Alps—solar forcing and evidence for variations in North Atlantic atmospheric circulation. *Quat. Sci. Rev.* 80, 112–128. <https://doi.org/10.1016/j.quascirev.2013.09.002>.
- Wong, H., Panin, N., Dinu, C., Georgescu, P., Rahn, C., 1994. Morphology and post-Chaudian (Late Pleistocene) evolution of the submarine Danube fan complex. *Terra. Nova* 6, 502–511. <https://doi.org/10.1111/j.1365-3121.1994.tb00894.x>.
- Wu, H., Guiot, J., Brewer, S., Guo, Z., 2007. Climatic changes in Eurasia and Africa at the last glacial maximum and mid-Holocene: reconstruction from pollen data using inverse vegetation modelling. *Clim. Dyn.* 29, 211–229. <https://doi.org/10.1007/s00382-007-0231-3>.
- Yanchilina, A.G., Ryan, W.B.F., McManus, J.F., Dimitrov, P., Dimitrov, D., Slavova, K., Filipova-Marinova, M., 2017. Compilation of geophysical, geochronological, and geochemical evidence indicates a rapid Mediterranean-derived submergence of the Black Sea's shelf and subsequent substantial salinification in the early Holocene. *Mar. Geol.* 383, 14–34. <https://doi.org/10.1016/j.margeo.2016.11.001>.
- Zaragosi, S., Bourillet, J.-F., Eynaud, F., Toucanne, S., Denhard, B., Van Toer, A., Lanfume, V., 2006. The impact of the last European deglaciation on the deep-sea turbidite systems of the Celtic-Armorican margin (Bay of Biscay). *Geo Mar. Lett.* 26, 317–329. <https://doi.org/10.1007/s00367-006-0048-9>.
- Zaragosi, S., Eynaud, F., Pujol, C., Auffret, G.A., Turon, J.-L., Garlan, T., 2001. Initiation of the European deglaciation as recorded in the northwestern Bay of Biscay slope environments (Meriadzek Terrace and Trevelyan Escarpment): a multi-proxy approach. *Earth Planet. Sci. Lett.* 188, 493–507. [https://doi.org/10.1016/S0012-821X\(01\)00332-6](https://doi.org/10.1016/S0012-821X(01)00332-6).